Mechanical evaluation of DIW-printed carbon nanofibers - Alumina-Toughened Zirconia composites

Vivian Inês dos Santos, Aziliz Ferey, Eva Chevalier, Márcio Celso Fredel, Bruno Henriques, Laurent Gremillard

Mechanical evaluation of DIW-printed carbon nanofibers - Alumina-Toughened Zirconia composites

This article has been published in
Journal of the European Ceramic Society (2024) Vol. 44, issue 15, article # 116745
https://doi.org/10.1016/j.jeurceramsoc.2024.116745

Vivian Inês dos Santos[a,b,*], Aziliz Ferey[b], Eva Chevalier[b], Márcio Celso Fredel[a], Bruno Henriques[a,c], Laurent Gremillard[b,*]

[a] Ceramic and Composite Materials Research Group (CERMAT), Federal University of Santa Catarina (UFSC), Campus Trindade, Florianópolis/SC, 88040-900, Brazil
[b] Univ Lyon, CNRS, INSA Lyon, UCBL, MATEIS, UMR5510, 69100 Villeurbanne, France
[c] CMEMS-UMinho, University of Minho, Campus de Azurém, 4800-058 Guimarães, Portugal
* Corresponding author. Tel: +55 48 3721-4591; fax: +55 48 3721-7615

E-mail address: vivian.inds@gmail.com (V. I. dos Santos); Laurent.gremillard@insa-lyon.fr (L. Gremillard)

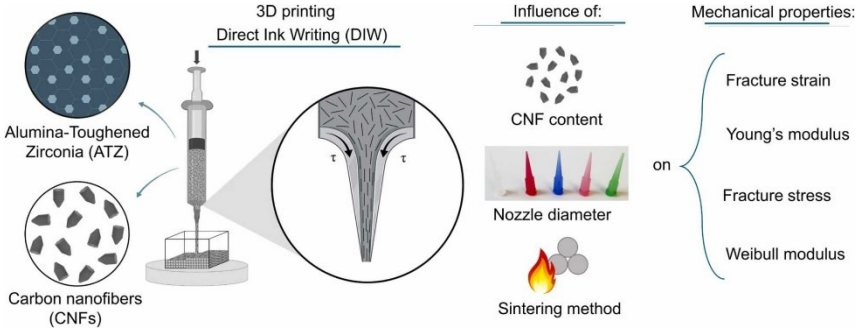

Abstract

Direct ink writing (DIW) offers cost-effective fabrication of intricate ceramic structures. However, the mechanical properties (reliability) of DIW-obtained components have been inadequate for structural applications. This study aimed to improve mechanical properties of DIW alumina-toughened zirconia (ATZ) composite filaments with and without carbon nanofibers (CNFs). Optimized debinding and sintering conditions were determined for Conventional Sintering (CS) and Spark Plasma Sintering (SPS). The influence of nozzle diameter, CNF content and sintering method on the fracture strain, Young's modulus, flexural strength and Weibull modulus was carefully assessed via correlation analyses. CNFs, although intended to enhance properties, were often agglomerated, which negatively affected mechanical properties. Smaller nozzle diameters enhanced Young's modulus, with CS-sintered ATZ filaments showing transformation-induced plasticity (TRIP). Mechanical properties rivaled or surpassed those of conventional techniques (*e.g.*, cold isostatic pressing, slip casting) with a good level of mechanical reliability achieved. Overall, DIW showed promise for ceramic materials, particularly ductile Ce-TZP-based composites.

Keywords:

alumina-toughened zirconia; carbon nanofibers; direct ink writing; additive manufacturing; mechanical reliability.

1. Introduction

Ceria-stabilized zirconia stands out as one of the most interesting ceramic materials in the field of biomedical applications. Its notable advantage arises from a stress-induced phase transformation, shifting from a tetragonal (t) to a monoclinic (m) phase. This transition brings about a significant volumetric expansion of ~4%, effectively impeding the propagation of cracks. Consequently, this mechanism greatly enhances the strength and toughness of tetragonal zirconia polycrystals (TZP) [1]. Another material that capitalizes on this stress-induced phase transformation is yttria-stabilized zirconia (Y-TZP). Ceria-stabilized zirconia (Ce-TZP) and Y-TZP are the most used materials among the TZP systems.

When comparing the two, Y-TZP demonstrates remarkable strength (800-1200 MPa) and a moderate level of toughness (~6 MPa·√m). In contrast, Ce-TZP typically exhibits extraordinarily high toughness (up to 15-20 MPa·√m) but limited strength (≤ 600 MPa). The latter arises from the challenge of producing dense Ce-TZP materials with small grain sizes (< 0.5 μm) [2], as the mobility of grain boundaries during sintering is considerably greater in Ce-TZP compared to Y-TZP [3]. Moreover, Ce-TZP ceramics display significantly reduced susceptibility to aging when compared to Y-TZP, owing to the presence of a tetravalent ion (Ce^{4+}) as the stabilizer. In addition, due to the exceptional transformability of Ce-TZP, notable non-linear, permanent ("plastic") deformation is observable before failure, with the most pronounced pseudoplastic/non-linear behavior among ceramic materials [4–8].

Consequently, significant research efforts have been directed toward incorporating an immiscible secondary phase to immobilize the grain boundaries and control grain growth within Ce-TZP [3,9,10]. Among these second-phase materials, alumina is by far the most explored. Various studies have developed Ce-TZP/Al_2O_3 composites [11–14], in which the addition of alumina demonstrated improvements in hardness, Young's modulus and fracture strength. However, it was noted that an increase in alumina content corresponded to a reduction in fracture toughness, aligning with the decrease in transformability. This type of material comprising zirconia and alumina (at higher and lower contents, respectively) is usually referred to as alumina-toughened zirconia (ATZ).

To further improve the mechanical properties, the introduction of elongated third-phase materials has been suggested. These elongated phases offer the potential to help hinder the growth of zirconia grains and further enhance toughness through mechanisms such as bridging and crack deflection [15–19]. Among the explored candidates for third-phase integration are strontium aluminate platelets (more specifically strontium hexaaluminate, $SrAl_{12}O_{19}$), initially investigated by Cutler *et al.* [6,7]. Their incorporation resulted in improved toughness and strength via crack branching and bridging mechanisms. However, it's worth noting that the composite with three phases also exhibited a reduced level of transformability in comparison to pure Ce-TZP ceramics. More recent investigations have been performed on this composition of three-phase composites [9,10,20]. Specifically, they have focused on 10.0-11.5Ce-TZP/Al_2O_3/$SrAl_{12}O_{19}$ composites with a volume ratio of 84/8/8. This particular configuration of Al_2O_3 and $SrAl_{12}O_{19}$ contents at 8 vol% was determined to yield the most refined microstructures post-sintering [9]. Notably, these composites demonstrated remarkable strength (> 1 GPa) and toughness (> 10 MPa·√m), accompanied by an exceptional flaw tolerance, resulting in a notably high Weibull modulus (m = 60) [20]. Given these favorable mechanical properties, the three-phase composite system (11Ce-TZP/Al_2O_3/$SrAl_{12}O_{19}$) with a volume ratio of 84/8/8 was selected for utilization in the present study.

In terms of processing methods, in recent years, additive manufacturing (AM) has gained significant attention and experienced rapid development. AM, also known as 3D printing, is a set of manufacturing techniques that construct computer-generated models by adding materials, typically layer by layer. It enables the production of complex geometries without the need for micromachining processes or costly molds. The utilization of AM technologies offers several distinct advantages, including rapid prototyping, predictable production, reduced assembly requirements, design flexibility, and the ability to meet specific customer requirements. Consequently, it has emerged as an attractive alternative to conventional manufacturing processes across various fields, including ceramics [21,22] – a field where traditional processing methods are limited by the need for special equipment and tooling as well as by the complexity of the molds.

There are diverse AM techniques available for fabricating ceramic structures, such as stereolithography (SLA), selective laser sintering (SLS), fused deposition modeling (FDM), inkjet printing, binder jet and direct ink writing (DIW or robocasting) [23–25]. Among these techniques, DIW stands out as a simple, emerging, cost-effective, environmentally friendly and rapid fabrication method. It enables the direct production of net or near-net complex-shaped ceramic structures with self-supporting properties and high aspect ratios by the extrusion of a paste through a printing nozzle. Nevertheless, the mechanical properties of ceramic materials produced through DIW require further improvements, particularly concerning their mechanical reliability, often expressed through Weibull modulus (m) values. To achieve better mechanical properties, this study suggests the incorporation of oriented carbon nanofibers (CNFs). This orientation would be possible by the shear stresses from the process of nozzle reduction during DIW printing (Figure 1)

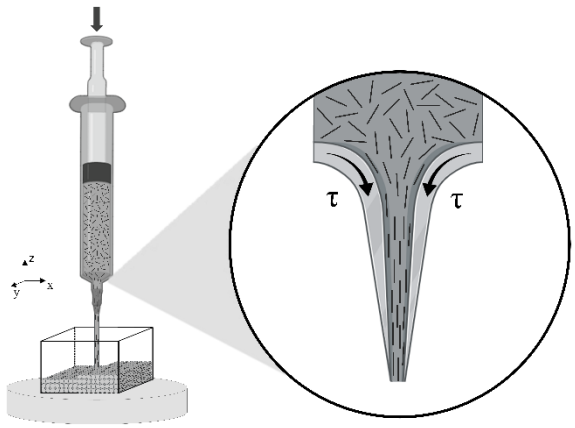

Figure 1. Schematic representation of the direct ink writing process and the orientation of elongated phases promoted by it. τ: shear stress.

Carbon nanofibers exhibit exceptional mechanical properties, elevated electrical and thermal conductivity and a remarkable strength-to-weight ratio [26]. Their incorporation has demonstrated enhancements in compressive strength, flexural strength, Young's modulus and fracture toughness [27–30]. By strategically orienting them in a specific direction, it is expected that these improvements could be further amplified through mechanisms such as microcrack bridging and crack deflection. Still, some challenges arise when adding carbon nanofibers to a ceramic matrix. These encompass the achievement of a homogeneous dispersion of the CNFs, their orientation during DIW printing and the sintering of the obtained component. To address the first, two methods were employed in this study: a deflocculant was added to the printing paste and a high-speed mixing technique was applied to the production procedure of the paste. The latter is a method that has already been utilized to achieve a homogeneous dispersion of CNFs in pastes for DIW [31].

Considering the orientation, this behavior observed in DIW happens as non-equiaxed particles tend to rotate and align themselves parallel to the shear direction under shear stresses [32]. This orientation phenomenon has been documented in DIW studies involving various materials, such as alumina particles [33], platelets [34], carbon nanofibers [31,35–37] and graphene nanoplatelets (GNP) [38]. According to Folgar-Tucker [32], the factors that affect these particles' orientation are the particles' shape (length/diameter ratio), interactions between these particles (particles' solid loading) and shear rate and time. The shear rate applied to the paste, particularly, is influenced by the nozzle diameter. This influence of the nozzle diameter on the maximum shear rate induced by the nozzle ($\dot{\gamma}_{max}$) is depicted in Eq. (1):

$$\dot{\gamma}_{max} = \frac{8 \cdot Q}{D} \qquad (1)$$

Where Q is the printing speed in mm/s (10 mm/s in this study) and D is the nozzle diameter in mm. As so, in this study, the nozzle diameter was assessed in terms of its influence on the orientation of the CNFs and the mechanical properties achieved.

Sintering with CNFs inside a ceramic also poses a significant challenge, because of the thermal decomposition of the CNFs in the presence of oxygen. The thermal stability and decomposition behavior of carbon nanofibers are the subject of ongoing research and the exact decomposition temperature range can differ based on the specific type of nanofibers, their structural properties, impurities, catalyst residues and surface functionalization. Nevertheless, there have been studies that have reported the thermal decomposition of the CNFs from 480-550 °C [39]. To address these difficulties and maintain the structural integrity of CNF materials while achieving sintering at reduced temperatures or shorter timeframes, the Spark Plasma Sintering (SPS) technique has been proven advantageous [40]. This method's high heating rate facilitates rapid completion of the sintering process, thereby minimizing potential damage to the CNF structures. To assess the impact of the process of SPS, a control group was established by conducting conventional sintering (CS).

Summarizing, this study aimed to improve the mechanical properties of ATZ composites by the addition of oriented CNFs. For that, the influence of CNF content, nozzle diameter and sintering method on the mechanical properties was evaluated. Processes that influence the final mechanical properties such as debinding and sintering were also carefully studied to reduce the likelihood of defects and ensure smaller grain sizes.

2. Materials and methods

2.1 Materials

The ATZ powder used in this study consists of 84 vol% Ce-TZP (11.0 mol% Ce), 8 vol% Al_2O_3, and 8 vol% $SrAl_{12}O_{19}$, which was obtained from Doceram® under the trade name "EvoCera®" in the form of a spray-dried powder. For deflocculation purposes, Darvan® 821-A from RT Vanderbilt® was employed, while Pluronic® F-127 from Sigma-Aldrich® served as the binder. The carbon nanofibers used in the experiments were Pyrograf®-III PR-19-PS and had diameters of 100-200 nm and lengths of 30-100 μm.

2.2 Methods

2.2.1 Preparation of the suspensions

The preparation of the pastes depicted in Figure 2 was carried out as follows. All mixing procedures were conducted in a SpeedMixer DAC 600 Hauschild® under a vacuum of 30 mBar, employing cycles of 800 rpm for 90 s, followed by 1500 rpm for 90 s. Initially, the deflocculant and deionized water were combined and zirconia mixing balls measuring 1 and 2 mm were introduced to facilitate the mixing process. Then, the binder was added and another round of mixing was performed. Subsequently, each mixing step was alternated with a cooling step of 10 min in a refrigerator at 4 °C. Once the binder was uniformly blended with the other components, the ATZ powder was introduced. Ten rounds of mixing and cooling were carried out to ensure optimal homogeneity. In cases where carbon nanofibers were included in the paste, they were added after the ATZ powder, followed by an additional ten cycles of mixing and cooling. Once the paste achieved homogeneity, the mixing balls were separated using a sieve. Before printing, the suspensions were put inside 5 mL syringes with a subsequent centrifugation step at 3000 rpm for 12 min to remove any bubbles.

Four groups were prepared with three different compositions that were later sintered either by conventional sintering (CS) or spark plasma sintering (SPS). The composition and sintering method of the groups evaluated in this study are displayed in Table 1.

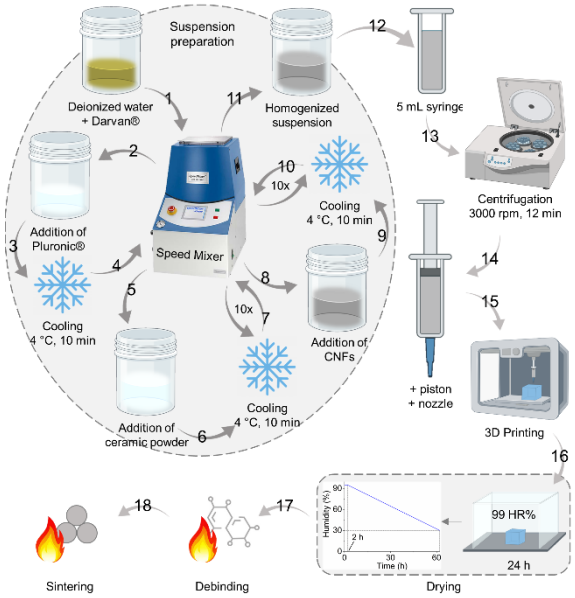

Figure 2. Schematic illustration of the obtention of the filaments, including the steps of paste preparation, printing and post-printing thermal processes.

Table 1. The four groups evaluated, their composition and sintering approach. (T): in relation to the total; (S): in relation to the solids (ATZ + CNFs); (L): in relation to the liquids (deionized water + Darvan); CS: conventional sintering; SPS: spark plasma sintering.

Group	ATZ	CNFs	Darvan® 821A	Pluronic® F-127	Deionized water	Sintering method
CS-ATZ	30 vol% (T)	–	1.0 wt% (S)	25 wt% (L)	Remaining quantity	CS
SPS-ATZ	30 vol% (T)	–	1.0 wt% (S)	25 wt% (L)	Remaining quantity	SPS
SPS0.5	30 vol% (T)	0.5 wt% (S)	1.0 wt% (S)	25 wt% (L)	Remaining quantity	SPS
SPS2	30 vol% (T)	2.0 wt% (S)	1.0 wt% (S)	25 wt% (L)	Remaining quantity	SPS

2.2.2 Obtention of the filaments

The filaments were printed via the Direct Ink Writing (DIW) method using a robocasting manufactured by 3D INKS, LLC® (Tulsa, USA) with nozzles of diameters of 200, 250, 410, 580 or 840 µm (Nordson®, Figure 3(a)). The printing procedure took place in an enclosure with 25 °C of temperature and 95% of humidity. The filaments were deposited on a glass plate on top of which a fine layer of coconut oil was previously applied to facilitate the detachment of the filaments. The printing speed utilized was 10 mm/s. For the nozzle diameters of 200, 250, 410, 580 and 840 µm, the nozzle offset (distance between the end of the nozzle and printing plate) was 230 (115%), 270 (108%), 450 (110%), 650 (112%) and 900 µm (107%), respectively. The printing pattern was a zig-zag (Figure 3(b)) leading to 25 mm long filaments (Figure 3(c)).

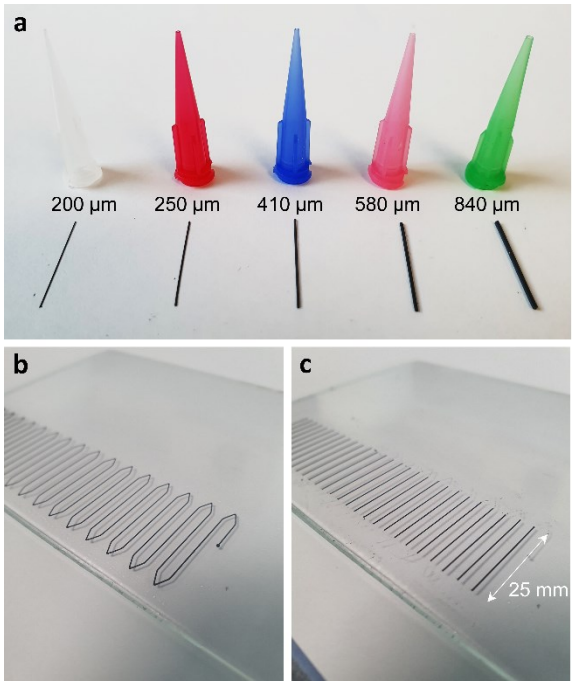

Figure 3. (a) The different nozzles used in this study with their corresponding diameters and obtained filaments. The color of the nozzles was utilized for the graphs of the filaments that were printed with each specific nozzle (gray for 200 µm, red for 250 µm, blue for 410 µm, pink for 580 µm and green for 840 µm). (b) Zig-zag printing pattern after printing and (c) after drying and cutting out the curves/edges.

The filaments, still on the glass plate, were dried in a climatic chamber (Weisstechnik® WKL 34/+10) at 25 °C (relative humidity of 95% for 2 h, then decreased to 30% over 60 h). After the drying process, the curves/edges of the zig-zag pattern were cut out with a cutter, the glass plate was heated to 30 °C on a hot plate to melt the coconut oil and the filaments were detached from the glass plate with the aid of a razor blade. Subsequentially, the filaments were placed in alumina crucibles (Figure S 1– Supplementary Material) and stored in a box with 30% relative humidity. After the debinding process, the filaments became extremely fragile (particularly those with smaller diameters) and any attempt to handle them directly would inevitably lead to breakage. Hence, the placement of the filaments inside crucibles was an essential procedure to ensure their protection due to the requirement to transfer them between the debinding and sintering furnaces.

2.2.3 Debinding study

The optimal debinding condition was determined by thermogravimetric analyses (TGA, SETARAM®) in an Argon atmosphere with a heating rate of 10 °C/min and a cooling rate of 30 °C/min. The samples were placed in an alumina crucible suitable for the equipment, on which a blank analysis was conducted. The resulting curve from this blank analysis was subtracted from the curves obtained during the analysis of the materials.

Two types of materials were examined: ATZ powder and small fragments of printed and dried filaments of ATZ with a 2.0 wt% content of carbon nanofibers (CNFs). The overall mass losses were evaluated up to 1300 °C with no plateau. Isotherms were also performed at 350°C and 400 °C with a 3 h plateau. The dried filament of ATZ with 2 wt% of CNFs had a nominal composition of 0.89 wt% of Darvan® 821A, 9.55 wt% of Pluronic® F-127, 1.80 wt% of CNFs and 87.76 wt% of ATZ powder. It is worth noting that small amounts of a polymer may be present in the ATZ powder as a result of its addition during the powder mixing process in an aqueous solution, followed by spray-drying. According to its datasheet, the Darvan has a boiling point of ~100 °C, hence should decompose around this temperature. According to the literature, the CNFs decompose approximately at 480-550 °C [39] (the exact temperature range is still debatable) and the Pluronic® F-127 decomposes between 200 and 400 °C (in nitrogen) [41].

2.2.4 Sintering study

The filaments utilized in this evaluation were previously debinded at 400 °C for 30 min. For this part of the study, filaments of 840 µm in diameter were either sintered by conventional sintering (CS) or by Spark Plasma Sintering (SPS). For the CS, only ATZ filaments (no CNFs) were sintered whereas, for the SPS, filaments with and without CNFs were sintered for comparison. To determine the optimal sintering temperature, the filaments were sintered by CS in a Pyrox® chamber furnace at 1350, 1400, 1450, 1500 or 1550°C, with a heating rate of 2.5 °C/min, cooling rate of 5 °C/min and a 1 h plateau. For the filaments sintered by SPS, the temperatures of 1350, 1400 and 1450°C were investigated (secondary vacuum, heating rate of 100 °C/min and 1 h plateau, furnace HP D25 from FCT®), without applied pressure (Figure S 2– Supplementary Material). The results of the sintering process were evaluated by density measurements and SEM images (Thermofischer® QuattroS equipment).

The density of the sintered filaments was determined via Archimedes' method (Eq. (2)) utilizing deionized water as the liquid phase. In the equation, ρ_{sample} is the measured density of the sintered filament, m_{dry} is the mass of the dry sample, m_{wet} is the mass of the wet sample, $m_{submerged}$ is the mass of the sample submerged in the liquid and ρ_{liquid} is the density of the liquid.

$$\rho_{sample} = \frac{m_{dry}}{m_{wet} - m_{submerged}} * \rho_{liquid} \qquad (2)$$

The relative density was calculated by the ratio of the measured density of the sample to the theoretical density calculated with the following values: the theoretical density of the ATZ powder considered was 5.8404 g/cm^3 and that of the CNFs was 2.16 g/cm^3. The value of relative density had an associated measurement uncertainty of ±2% linked to the precision of the scale utilized (0.0001 g) and the very low weight of the filaments (0.0147-0.0221 g).

2.2.5 Mechanical study under flexion of filaments

The printed filaments were mechanically characterized by 3-point flexural tests in a BOSE EF3200 multi-test machine with a 20 N force cell, displacement sensor LVDT (linear variable differential transformer) with 50 nm displacement resolution and 15 mm lower span distance (Figure 4(a)). For the samples utilized in this test, the CS process was done at 1500 °C for 1 h, whereas the SPS process was performed at 1400 °C for 1 h. The evaluated groups were the same as those displayed in Table 1 (CS-ATZ, SPS-ATZ, SPS0.5 and SPS2) and, in each group, 30 filaments were tested.

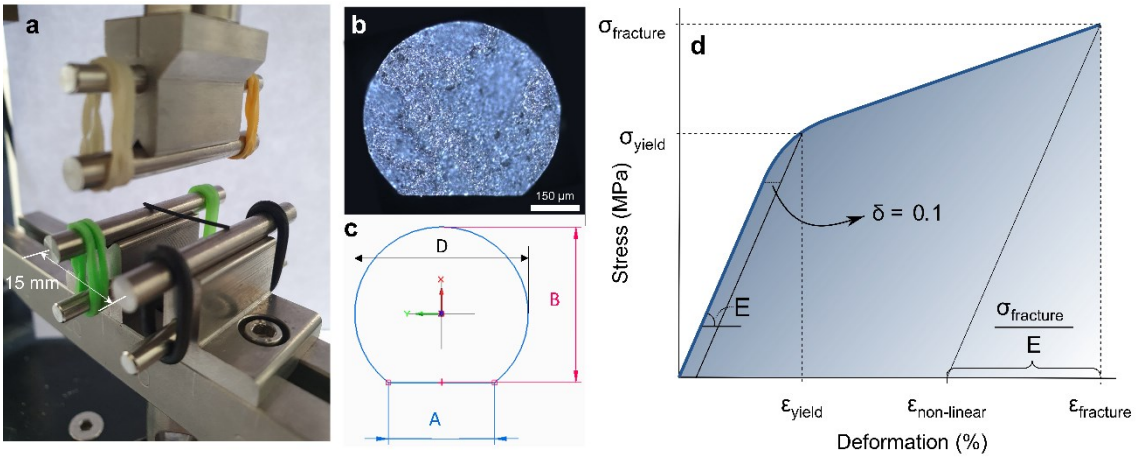

Figure 4 (a) 3-point bending device utilized for the mechanical evaluations. (b) Optical microscopy image of the cross-section of a printed filament and (c) schematic representation of the diameter (D) and dimensions A and B used for the calculation of the quadratic moment. (d) Schematic illustration of how the characteristic values were obtained from the stress vs. deformation curves.

The stress-strain curves were deduced from the load-displacement curves using the following method. The stress (σ) and strain (ε) were calculated from the applied load (F) and displacement (u_x) using Eq. (3), (4) – Castigliano theorem – and (5):

$$\sigma = \frac{F \cdot L \cdot x}{4 \cdot I_y} \quad (3)$$

$$u_x = \frac{L^3 \cdot F}{48 \cdot E \cdot I_y} \leftrightarrow E = \frac{L^3 \cdot F}{48 \cdot u_x \cdot I_y} \quad (4)$$

$$\varepsilon = \frac{\sigma}{E} = \frac{F \cdot L \cdot x}{4 \cdot I_y} \cdot \frac{48 \cdot u_x \cdot I_y}{L^3 \cdot F} = \frac{12 \cdot u_x \cdot x}{L^2} \quad (5)$$

Where L is the length between cylinders (lower span, 15 mm, in this case), E is the Young's modulus, x is the distance from the tensile side of the filament to the neutral axis and I_y is the quadratic moment. As the printed filaments have a flat side where they touched the printing substrate, their quadratic moment is not that of a round filament. Hence, I_y and x were calculated individually for each tested filament by SolidEdge® after measurements of thickness (dimension A) and height (dimension B) of each filament by optical microscopy (Figure 4(b) and (c)). The value of Young's modulus (E) was directly calculated as the slope of the linear part of the stress-strain curve.

From the stress-strain curves, a few key characteristic mechanical values were defined as shown in Figure 4(d). Whenever the behavior was not purely linear elastic, the yield stress (σ_{yield}) was defined as the stress necessary to reach δ = 0.1% of plastic deformation, corresponding to a yield strain ε_{yield}. Fracture stress ($\sigma_{fracture}$) was defined as the maximum stress attained before fracture; the corresponding strain was denoted as $\varepsilon_{fracture}$. In addition, a non-linear strain ($\varepsilon_{non\text{-}linear}$) was calculated by removing the elastic part of the strain from the fracture strain (Eq. (6)):

$$\varepsilon_{non-linear} = \varepsilon_{fracture} - \frac{\sigma_{fracture}}{E} \quad (6)$$

A Weibull analysis was also conducted on each group, utilizing Eq. (7):

$$F = 1 - \exp\left(\frac{-\sigma_f}{\sigma_0}\right)^m \quad (7)$$

Where F is the probability of failure ($0 < F < 1$) under applied stress σ_f, whereas σ_0 is the characteristic strength of the material. The Weibull modulus (m) was determined by the slope of the curve $\ln\left(\ln\left(\frac{1}{1-F}\right)\right)$ *vs.* $\ln(\sigma_f)$.

In addition, after observing a certain inelastic deformation in the filaments that underwent conventional sintering, these were tested in flexural cycles. This was done by applying five cycles of increasing imposed force at regular intervals aiming to achieve the maximum deformation while avoiding sample breakage (force intervals from 0.3-0.4 to 2.0-4.2 N). Intermediary and larger nozzle sizes were preferred for the evaluation under flexural cycles to enable a more comprehensive observation of results with an increased volume of material. In another test, six cycles with the same imposed force (from 0.37 to 2 N) were applied to study fatigue on the filaments. SEM evaluations of the filaments' surface were also conducted on conventionally sintered filaments tested under flexion where the test was stopped right before failure.

2.3 Data analysis

Results were expressed as mean value ± standard deviation and were statistically analyzed using ONE-WAY Analysis of Variance (ANOVA). The influence of the variables CNF content, nozzle diameter and sintering method was evaluated in relation to the fracture strain and stress and Young's and Weibull moduli values by correlation and regression analysis. A correlation was established by a value higher than |0.25| and differences were considered significant if p-value ≤ 0.05. The percent chance that there was a true relationship between the variables was calculated by CTR (chance of true relationship) = (1 – p-value) x 100. The 95% interval of confidence of the Weibull modulus was calculated according to the study of Griggs *et al.* [42].

3. Results

3.1 Debinding study

Multiple approaches exist to create an aqueous paste with optimal rheology for DIW to obtain a ceramic component. Frequently, organic additives are incorporated into the suspensions to facilitate the preservation of the printed geometry through polymer chain bridging [43–45], an incorporation that requires a post-printing debinding step – some studies avoid the debinding process by reducing the volume of organics in the paste composition [46–49]. In this study, in addition to the ATZ powder and CNFs, a deflocculant (Darvan® 821-A), a binder (Pluronic® F-127) and deionized water composed the printing paste. Hence, after drying, a debinding study was performed to define the best condition to remove the organic material without damaging the printed structure. The results of the TGA analyses of ATZ powder and a dried filament obtained from the paste containing 2 wt.% CNFs are displayed in Figure 5.

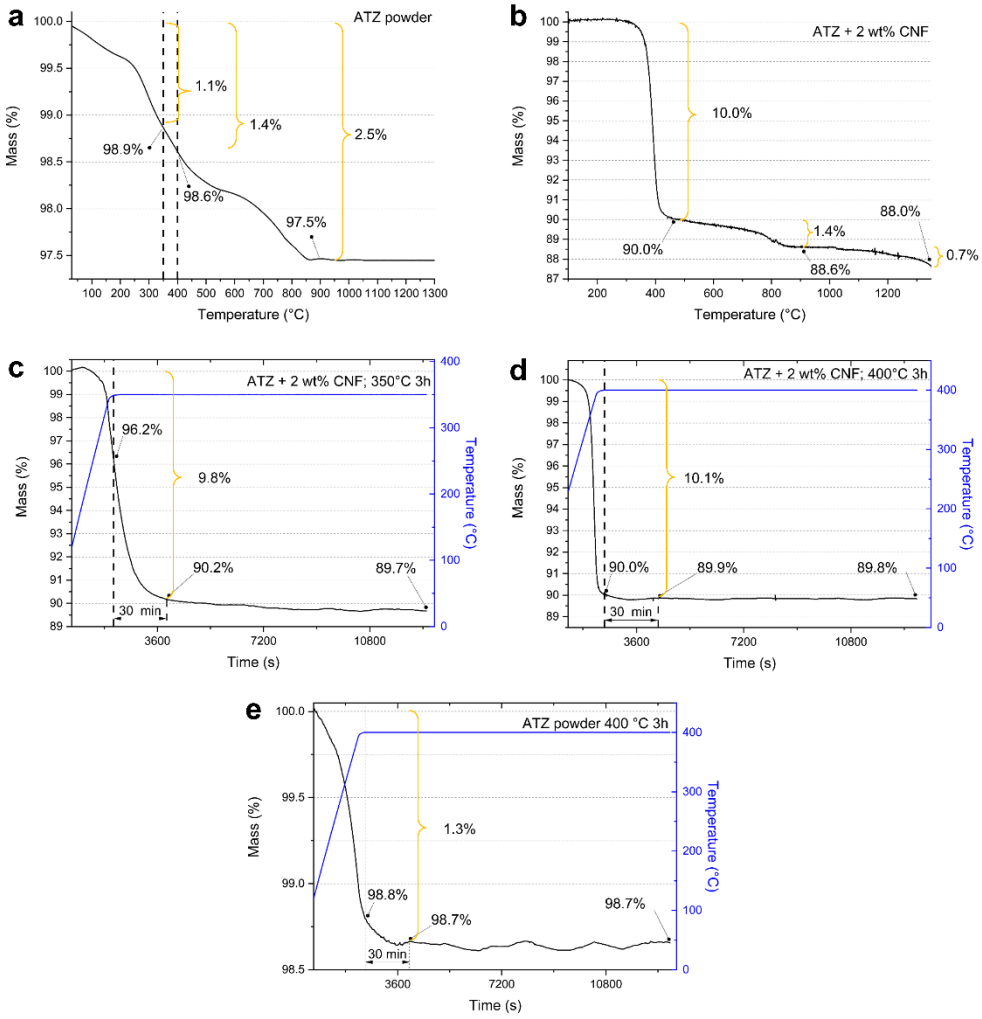

Figure 5. TGA analyses to determine the debinding temperature. Evolution of the mass with increasing temperature for the (a) ATZ powder up to 1300 °C and (b) ATZ with 2 wt% of CNFs up to 1300 °C. Evolution of the mass with time for the group of ATZ with 2 wt% of CNFs when treated at (c) 350 °C for 3 h and (d) 400 °C for 3 h. (e) Evolution of the mass with time for the ATZ powder treated at 400 °C for 3h. ***(1.5-column fitting)***

The TGA analysis of the ATZ powder (Figure 5(a)) revealed the presence of residual polymer in the powder, as indicated by a continuous decrease in mass up to 900 °C (followed by a stable mass value up to 1300 °C). The total mass loss was 2.5%, with values of 1.1% and 1.4% up to 350 °C and 400 °C, respectively. This mass loss cannot be attributed to any of the ceramic materials present (Ce-TZP, Al_2O_3 and $SrAl_{12}O_{19}$), as the evaluated temperatures are not sufficiently high to affect them. Hence the inference that the presence of a polymer caused these reductions.

Regarding the ATZ with 2.0 wt% of CNFs (Figure 5(b)), a significant mass reduction of 10.0% occurred around the temperature range of ~350-400 °C. A smaller decrease of 1.4% was further observed up to 900 °C, followed by an additional decrease of 0.7% with further temperature increase. The mass loss at 350-400 °C is mostly attributed to the decomposition of Pluronic [41]. Although CNFs decompose in the temperature range of 480-550 °C [39], no CNF decomposition is expected as the analyses were conducted in an argon atmosphere. The second mass decrease of 1.4% was mostly attributed to the decomposition of the residual polymer within the ATZ powder (in agreement with the mass loss observed on the ATZ powder), although the Pluronic may also have contributed. The third decrease (0.7%, over 900 °C) was likely entirely linked to the decomposition of residual Pluronic. Overall, Figure 5(b) shows no sign of CNF decomposition at high temperatures.

Considering that the extraction of the majority of Pluronic occurs in the range of 350-400 °C, two conditions were taken into account for the debinding process, which were, therefore, assessed through TGA analysis: heating up to 350 °C with a 3-hour plateau at this temperature (Figure 5(c)) and heating up to 400 °C, also with a 3-hour plateau (Figure 5(d)). After 3 h at 350 °C, a total weight loss of ~10% was measured, which hints at a ~2 wt% residual organic phase. The same result was obtained after only 30 min at 400 °C, with no further mass loss at this temperature. The ATZ powder was analyzed under the same conditions (Figure 5(e)). A mass loss of 1.3% took place after 30 minutes at 400 °C. No further mass loss occurred. This shows that the 2 % organic residue deduced from Figure 5(d) is a mix of Pluronic and binder from the initial powder (or decomposition products of these organic components). This remaining organic phase is likely to decompose during the subsequent sintering procedure, posing a low potential for defect generation as it leaves the samples.

3.2 Sintering study

The sintering study encompassed density and morphological evaluations. The density results are presented in Table 2 for both sintering approaches: conventional sintering (CS) and Spark Plasma Sintering (SPS).

Table 2. *Density results of the sintering study with different sintering methods/approaches and temperatures. $T_{sintering}$: temperature of the sintering plateau; $t_{sintering}$: time at the plateau.*

Sintering approach	Sample	$T_{sintering}$ (°C)	$t_{sintering}$ (h)	Measured density	Theoretical density	Relative density
CS	ATZ	1350	1	5.40	5.84	92.4
	ATZ	1400	1	5.49	5.84	93.9
	ATZ	1450	1	5.59	5.84	95.7
	ATZ	1500	1	5.73	5.84	98.0
	ATZ	1550	1	5.76	5.84	98.6
SPS	ATZ	1350	1	5.37	5.84	91.9
	0.5 wt% CNF		1	5.33	5.79	92.0
	ATZ	1400	1	5.73	5.84	98.0
	0.5 wt% CNF		1	5.73	5.79	99.0
	ATZ	1450	1	5.66	5.84	97.0
	0.5 wt% CNF		1	5.57	5.79	96.2

In the conventional sintering (CS), the relative density of the ATZ samples increased with increasing temperatures ranging from 92 to 99% for the 1350 and 1550 °C, respectively. Nevertheless, the high relative uncertainty (±2%, due to the very small size of the samples) should lead to trust more the tendency shown by these values (*i.e.* increased relative density with increasing sintering temperature) than the raw values themselves. Using Spark Plasma Sintering (SPS), sintering at 1350 °C resulted in densities of approximately 91-92%, while an optimal density of 98-99% was reached at 1400 °C and further increasing the sintering temperature (up to 1450 °C) led to lower densities (96-97%).

However, these values fall within the respective error ranges, failing to reach a significant difference. The inclusion of 0.5 wt% of carbon nanofibers (CNFs) did not affect significantly the densification.

To further understand the effect of the sintering temperatures, morphological evaluations were performed on the sintered samples. The outcomes of this evaluation, alongside the density results, assisted in the definition of the sintering temperature for both approaches. The microstructural images of the sintered samples are depicted in Figure 6 for the CS method and in Figure 7 for the SPS approach. The grain size evaluation of the sintered samples is displayed in Figure 8.

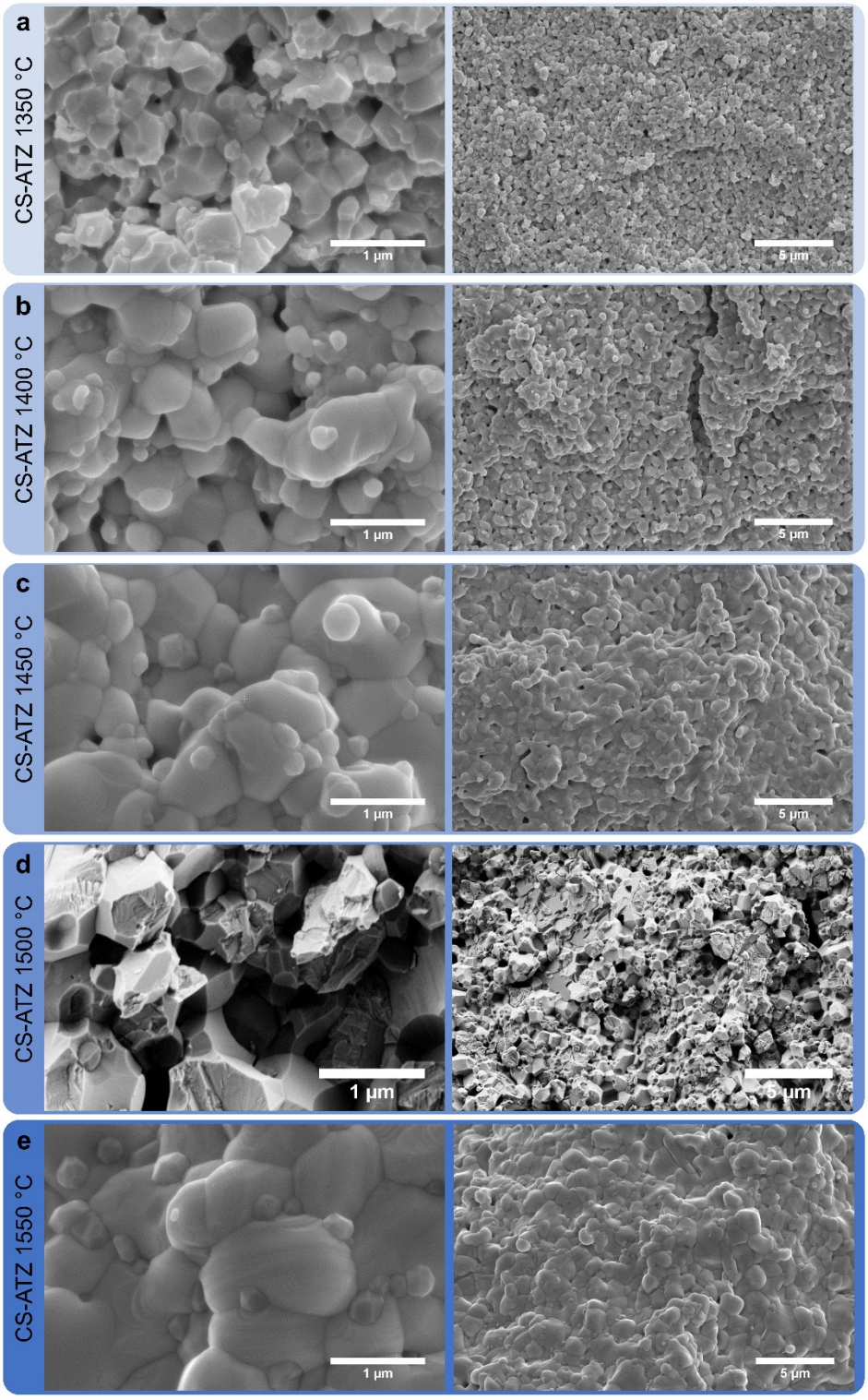

Figure 6. Microstructural evaluation of ATZ filaments sintered by Conventional Sintering (CS). Sintering at (a) 1350, (b) 1400, (c) 1450, (d) 1500 or (e) 1550 °C. It is possible to notice larger zirconia grains with smaller alumina grains predominantly at the grain boundaries.

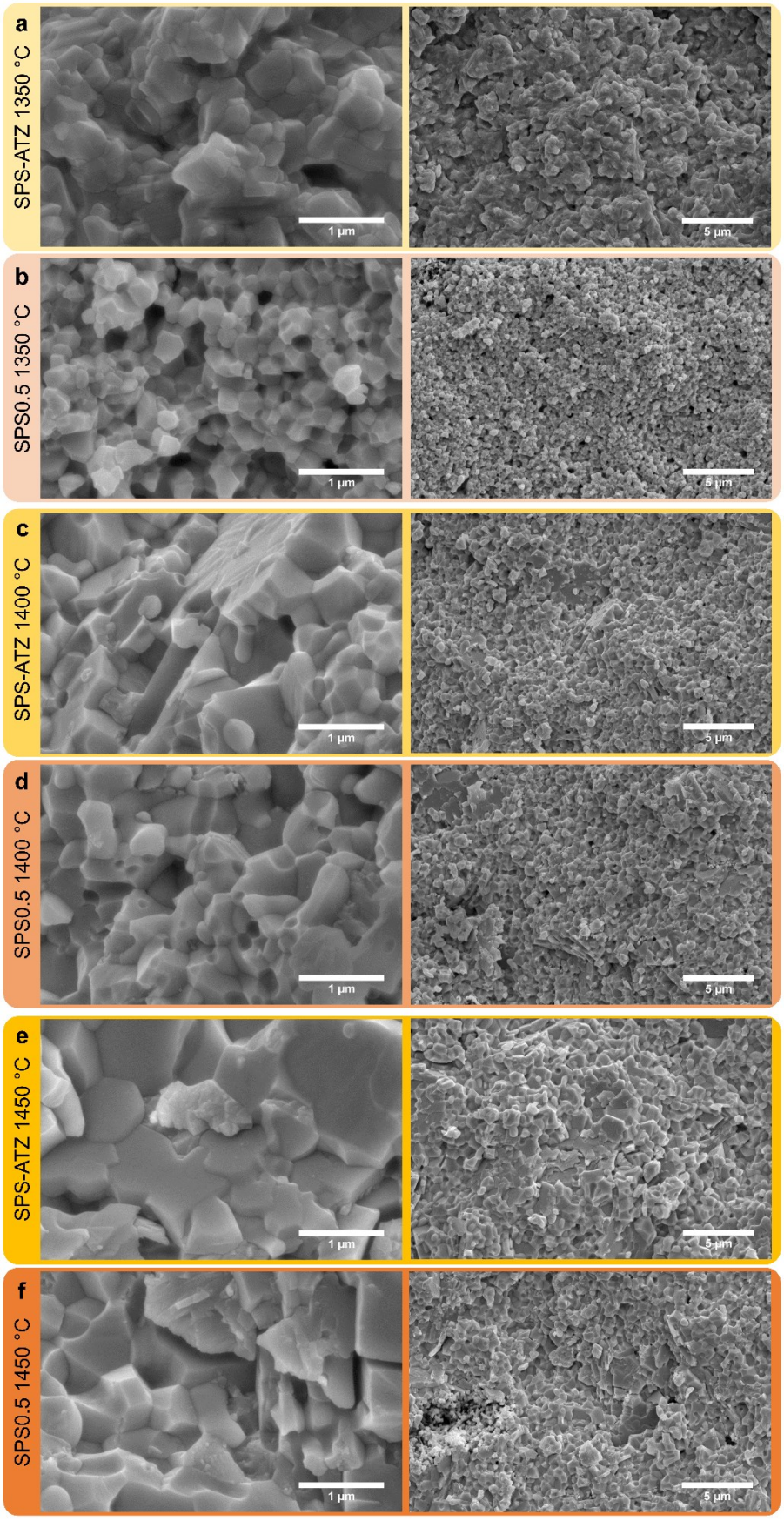

Figure 7. Microstructural evaluation of filaments sintered by Spark Plasma Sintering (SPS). ATZ filaments in yellow (a, c and e) and ATZ with 0.5 wt% of CNFs in orange (b, d and f). Sintering at (a and b) 1350, (c and d) 1400 or (e and f) 1450 °C

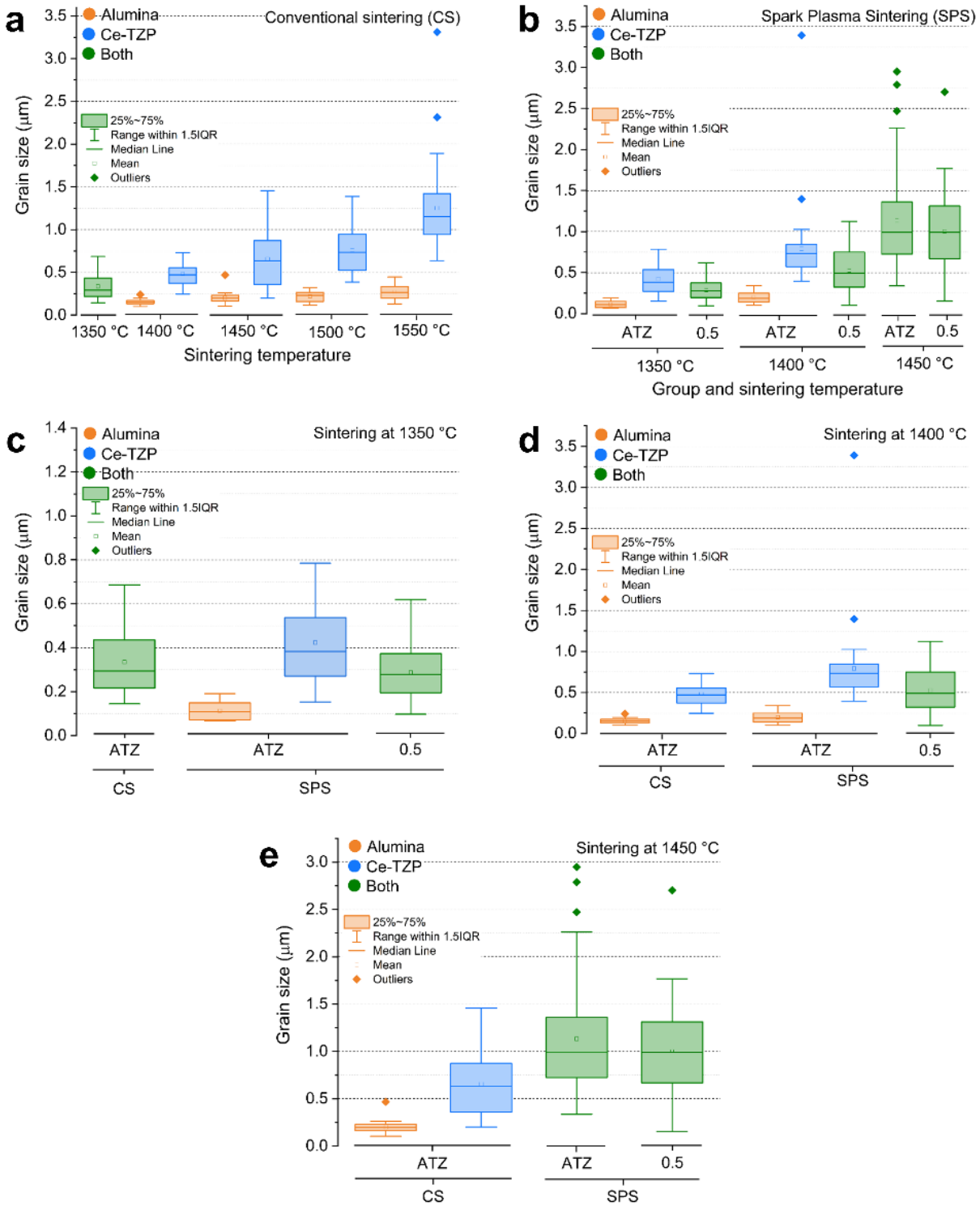

Figure 8. Grain size evaluation for (a) ATZ samples sintered by conventional sintering and (b) ATZ and ATZ with 0.5 wt% CNF samples sintered by Spark Plasma Sintering. Comparison of the grain sizes obtained by CS and SPS at (c) 1350, (d) 1400 and (e) 1450 °C. The orange color represents alumina grains, whereas the blue color represents Ce-TZP grains. In some samples, it was not possible to visually distinguish the alumina (usually smaller and more angular) from the Ce-TZP grains – the green color represents these samples and contains the sizes of both kinds of grains. When it was not possible to distinguish the alumina and zirconia grains in one group, the comparison with a second group was made in relation to the average grain size of alumina and zirconia together, regardless of whether in that second group it was possible to distinguish the grains.

Larger grains and significantly less number of pores were observed for both sintering approaches as the sintering temperature increased. For the conventionally sintered (CS) samples (Figure 8(a)), the increase in the size of alumina grains was less pronounced than that of Ce-TZP grains. Samples sintered at 1500 °C had a higher mean value of Ce-TZP grain size compared to those sintered at 1450 °C, with a similar grain size range. However, at a slightly higher temperature of 1550 °C, very large grains (~2.3

and ~3.3 µm) were present. In terms of density, the CS samples sintered at 1500 and 1550 °C exhibited the highest densities (98 and 99%, respectively). Therefore, because of the smaller grain sizes, 1500 °C was the selected temperature for the CS approach.

For the Spark Plasma Sintering (SPS) method, a similar trend of increasing grain sizes with higher temperatures was observed, with samples containing 0.5 wt% CNFs exhibiting slightly smaller grain sizes compared to those without CNFs. Additionally, in all CNF-containing samples, it was not possible to distinguish between the alumina and Ce-TZP grains. Samples sintered by SPS at 1400 °C had smaller mean values and narrower ranges than those sintered at 1450 °C. This, coupled with the higher density values observed in the 1400 °C samples (~98-99%) compared to the 1450 °C samples (~96-97%), supported the decision to select 1400 °C as the sintering temperature for the SPS approach. It should also be observed that samples sintered by SPS had higher mean values of grain size and wider ranges (Figure 8(c-e)), a fact that could harm the mechanical properties and will be a topic of discussion in the upcoming sections.

During the microstructural evaluations conducted to optimize the sintering process, it was noted that the samples containing CNFs exhibited their agglomeration (Figure 9). The presence of CNF agglomerates is expected to have a detrimental effect on the mechanical properties, which will be assessed in the subsequent sections and on density since the CNFs form very porous agglomerates with no ceramic inside (however, this effect was not observed (Table 2)).

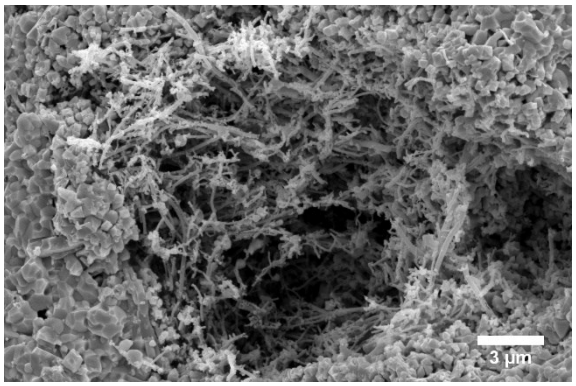

Figure 9. SEM image evidencing the agglomeration of CNFs in samples containing 0.5 wt% CNF.

3.3 Mechanical study

3.3.1 Stress vs. deformation graphs

The curves of stress *vs.* deformation for a single sample from each group are illustrated in Figure 10. The key characteristic mechanical values for all 30 samples within each group are presented in Figure 11, which were utilized for group-to-group or nozzle-to-nozzle comparisons. The characteristic properties of the non-linear behavior of CS-ATZ samples are shown in Table 3.

Table 3. *Non-linear mechanical properties of the CS-ATZ filaments by the nozzle diameter utilized in the printing process. $\varepsilon_{non\text{-}linear}$: non-linear strain; ε_{yield}: yield strain; σ_{yield}: yield stress. Check Figure 4(d) for further clarification.*

	Nozzle diameter (µm)				
	200	**250**	**410**	**580**	**840**
$\varepsilon_{non\text{-}linear}$ (%)	0.75 ± 0.07	1.02 ± 0.07	0.68 ± 0.09	0.70 ± 0.10	0.84 ± 0.07
ε_{yield} (%)	0.27 ± 0.01	0.22 ± 0.01	0.27 ± 0.02	0.35 ± 0.05	0.31 ± 0.03
σ_{yield} (MPa)	526 ± 71	396 ± 15	561 ± 29	594 ± 46	490 ± 6

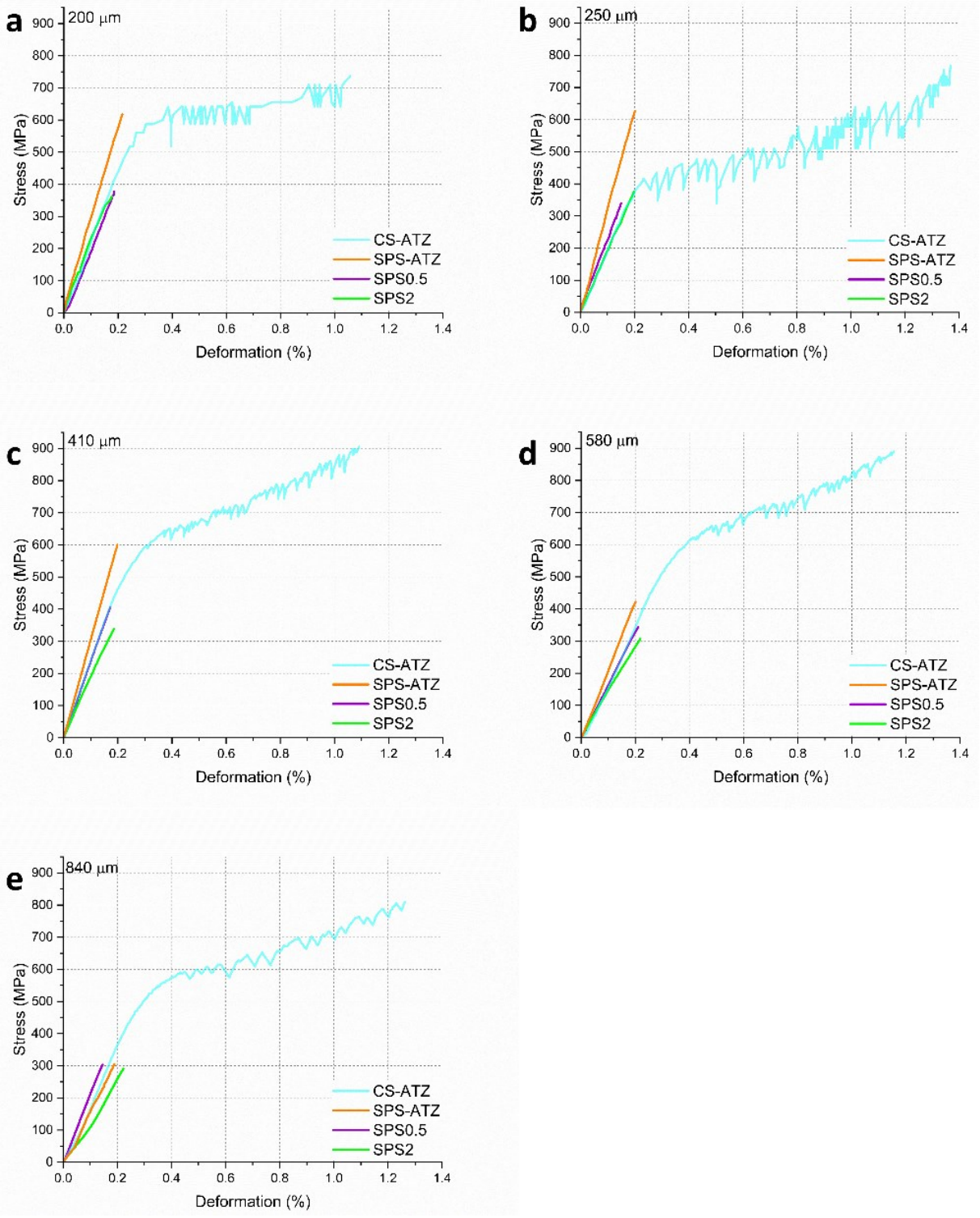

Figure 10. Stress vs. deformation for the groups CS-ATZ, SPS-ATZ, SPS0.5 and SPS2 and printed with nozzles of diameters of (a) 200, (b) 250, (c) 410, (d) 580 and (e) 840 µm.

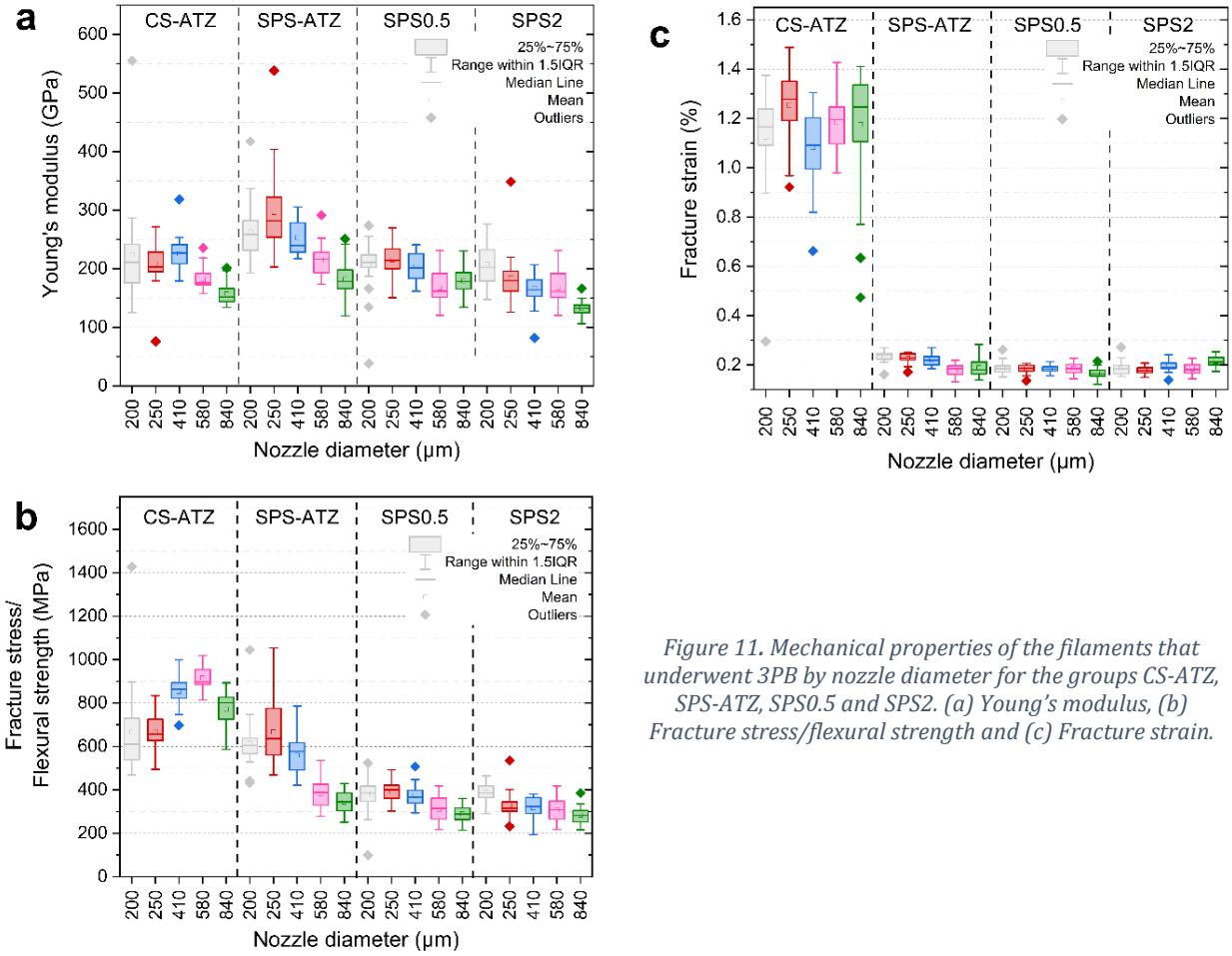

Figure 11. Mechanical properties of the filaments that underwent 3PB by nozzle diameter for the groups CS-ATZ, SPS-ATZ, SPS0.5 and SPS2. (a) Young's modulus, (b) Fracture stress/flexural strength and (c) Fracture strain.

Influence of the composition and sintering method

It's noticeable that the SPS-ATZ group consistently displayed the highest Young's modulus values (depicted in Figure 11(a)), while the SPS2 group exhibited the lowest values, with a noticeable tendency of reduction in the Young's modulus with the addition of CNFs. Regarding the fracture stress/flexural strength, upon analyzing the filaments obtained using 200, 250 and 410 μm nozzles, it was evident that both the CS-ATZ and SPS-ATZ groups exhibited higher values compared to the SPS0.5 or SPS2 groups (Figure 11(b)). This observation supports the expectation that the agglomeration of CNFs indeed impairs flexural strength. In the case of filaments produced using 580 or 840 μm nozzles, the CS-ATZ group demonstrated higher fracture stresses compared to all other groups. In summary, the agglomeration of CNFs negatively affected flexural strength across all nozzle diameters. Notably, with larger nozzles (580 and 840 μm), ATZ filaments sintered via SPS exhibited lower flexural strength than those sintered using CS.

When examining the fracture strain (depicted in Figure 11(c)), the CS-ATZ group exhibited significantly higher fracture strains compared to the other groups. Indeed, only the CS-ATZ samples displayed inelastic/non-linear deformation, while all other groups exhibited only elastic deformations (Figure 10) as expected from most ceramics. Among these three groups, the SPS-ATZ group demonstrated a higher fracture strain when using the 200 μm printing nozzle, with no significant difference observed between the SPS0.5 and SPS2 groups. However, when using other printing nozzles, there were no significant differences among these three groups in terms of fracture strain.

Influence of the printing nozzle diameter

Regarding the Young's modulus, in general, when sintered by SPS, the smaller nozzles produced filaments with higher Young's modulus (Figure 11(a)). However, for filaments that underwent sintering by CS, there was no clear trend regarding the influence of nozzle diameter on Young's

modulus. In terms of the fracture stress (Figure 11(b)), the only discernible trend was that for ATZ filaments sintered by SPS, for which smaller nozzles produced filaments with higher flexural strength. Furthermore, there was no clear trend observed in terms of fracture strains when varying the printing nozzle diameter (Figure 11(c)).

Inelastic deformation of the CS-ATZ filaments

As could be observed in Figure 10, the CS-ATZ filaments undergo both elastic and inelastic deformations. The value of fracture strain ($\varepsilon_{fracture}$) of this group was around 1.2%. When the elastic component is removed, the non-linear strain value ($\varepsilon_{non\text{-}linear}$) is approximately 0.7-0.8% (

). It is noteworthy that the values of yield strain (ε_{yield}) for the CS-ATZ filaments (ranging from 0.22 to 0.35% on average) are close to the $\varepsilon_{fracture}$ values for the SPS-ATZ filaments (ranging from 0.20 to 0.24% on average, see

). This deformation will be further investigated in section 3.3.3, particularly to determine whether it is plastic in nature or associated with the formation of microcracks.

3.3.2 Mechanical reliability – Weibull analysis

The reliability of the mechanical evaluations performed can be assessed via the Weibull modulus, which was calculated and is present in Figure 12. In terms of individual values, the lowest Weibull modulus recorded was 5.8, observed in the SPS-ATZ filaments printed with 250 µm nozzles. On the other hand, the highest Weibull modulus observed was 20.1, which was associated with CS-ATZ filaments printed using 580 µm nozzles. The majority of Weibull moduli found stay between 8 to 11 – values that underline the good mechanical reliability of the printed filaments. Similar to the previous sections, the influence of composition, sintering approach and printing nozzle diameter on the reliability of the mechanical evaluations can be analyzed.

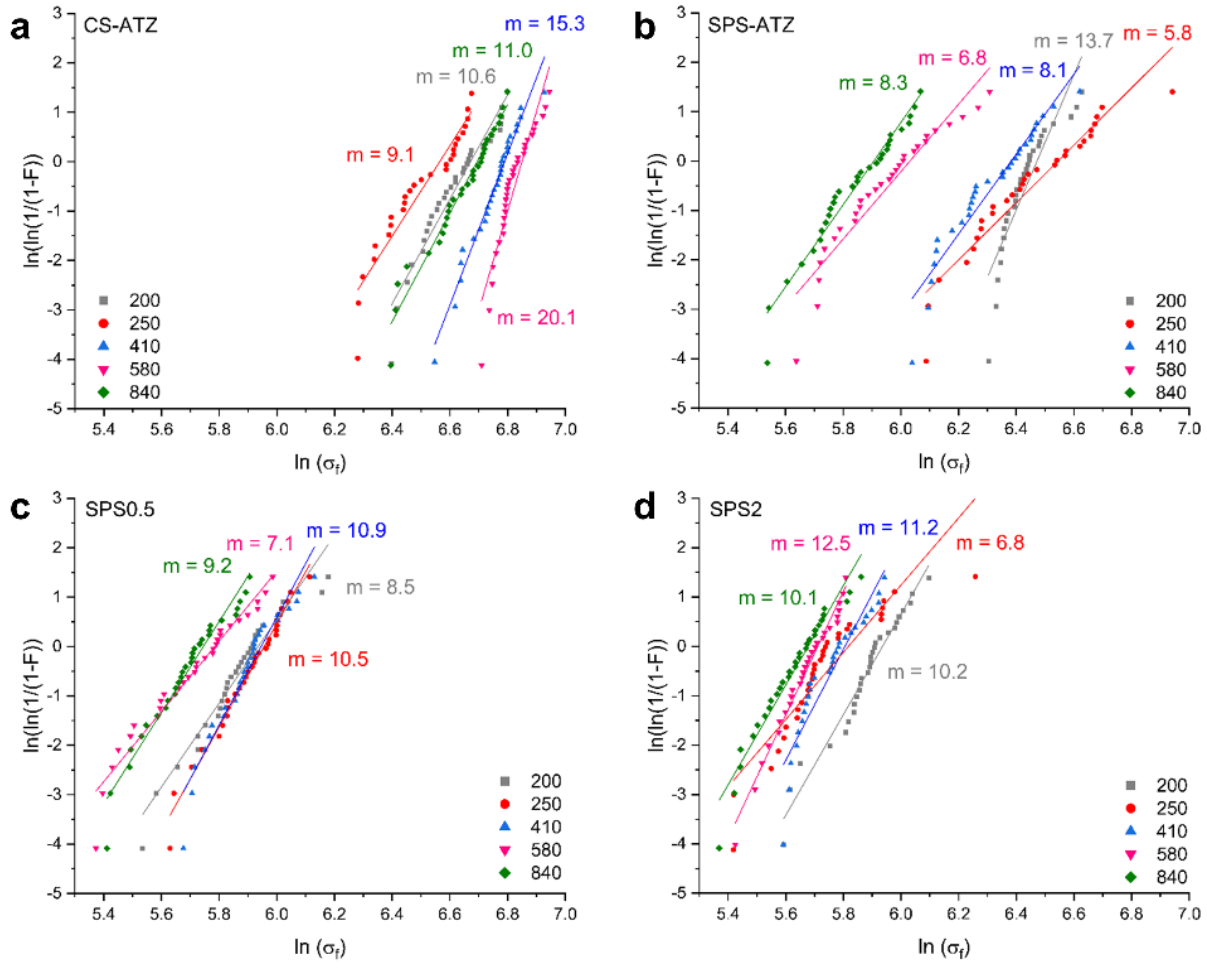

Figure 12. Results of the Weibull analysis. ln(ln(1/(1-F)) vs. ln(σ_f) for different nozzle diameters in the groups (a) CS-ATZ, (b) SPS-ATZ, (c) SPS0.5 and (d) SPS2.

Influence of the composition and sintering method

Analyzing the Weibull modulus by nozzle diameter, the scenario is as follows (from the highest value to the lowest):

- 200 µm: SPS-ATZ > CS-ATZ > SPS2 > SPS0.5;
- 250 µm: SPS0.5 > CS-ATZ > SPS2 > SPS-ATZ;
- 410, 580 and 840 µm: CS-ATZ > SPS2 > SPS0.5 > SPS-ATZ.

In summary, the CS-ATZ group was associated with higher Weibull moduli, indicating greater mechanical reliability, while the SPS-ATZ group exhibited lower Weibull moduli, indicating relatively lower mechanical reliability.

Influence of the printing nozzle diameter

The main trend observed is that the 250 µm nozzles exhibited the lowest mechanical reliability in three out of the four groups (CS-ATZ, SPS-ATZ and SPS2). However, this trend does not apply to the only nozzle diameter smaller than 250 µm (200 µm).

3.3.3 Transformation-induced plasticity (TRIP)

Based on the observations made on the flexural curves of the CS-ATZ filaments, it was decided to conduct cyclic three-point flexion at regular intervals, taking into account the maximum force that could be applied to these filaments. The force *vs.* displacement curves for the filaments printed with 410 and 840 µm are presented in Figure 13(a) and (b), along with the calculated slopes for the descending portion of each cycle. Additionally, a photograph of the filaments before and after this test is shown in Figure 13(d).

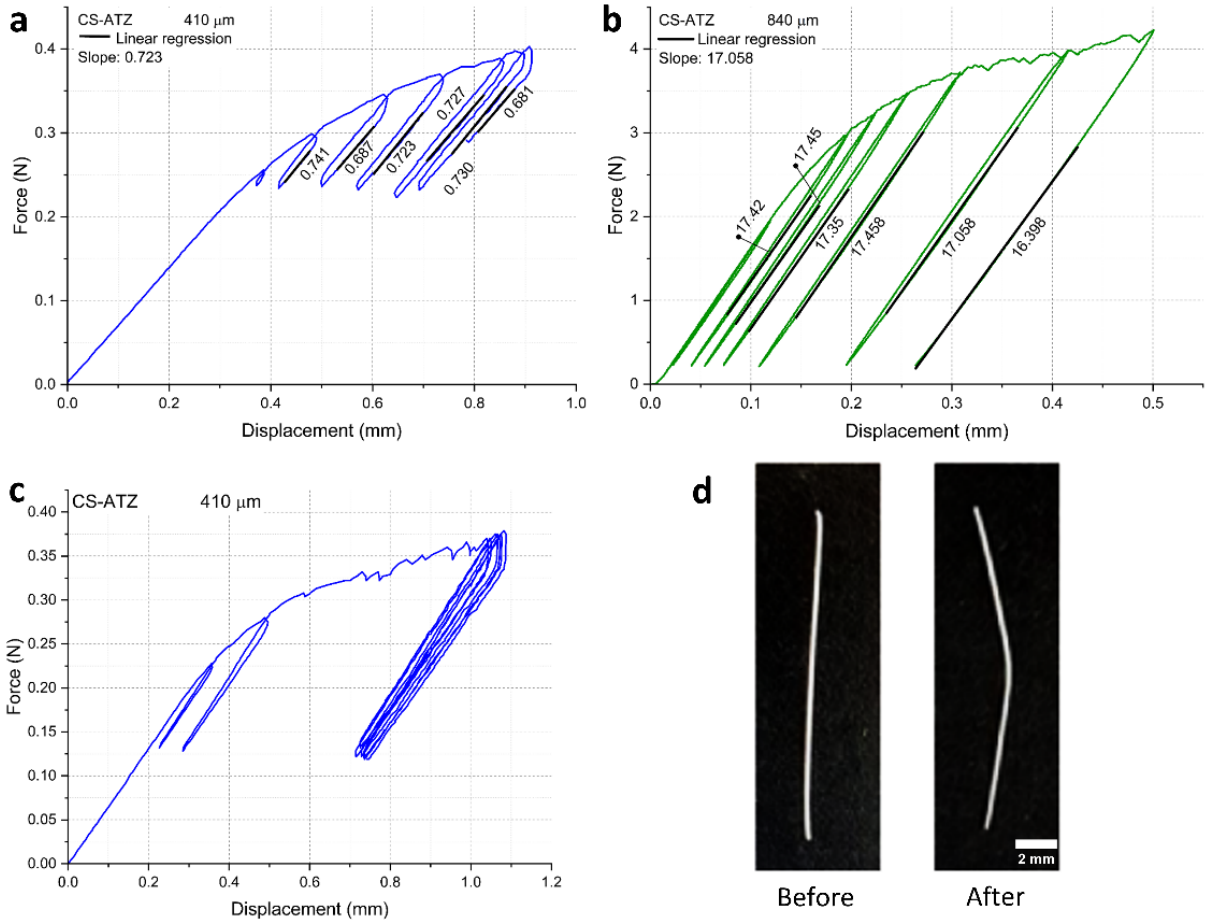

Figure 13. Cyclic three-point flexural results. Force vs. displacement for CS-ATZ filaments printed with nozzle diameters of (a) 410 and (b) 840 µm that underwent cycles of deformation. (c) Force vs. displacement for CS-ATZ filaments printed with nozzle diameters of 410 µm that underwent cycles with a constant applied load. (d) Photograph of a CS-ATZ filament that had been

printed with a 410 µm nozzle before and after undergoing cycles of deformation. It is possible to observe the expressive inelastic deformation presented by the CS-ATZ filaments after 3PB and before fracture. ***(1.5-column fitting)***

Based on the findings shown in Figure 13(a) and (b), it can be observed that there was a minimal reduction in Young's modulus (slope) between the cycles, with only a slight decrease occurring just before filament fracture. This suggests that the phenomenon of microcracking did not occur within the filaments before the last cycle. Similarly, flexural cycles were conducted with a constant applied load (Figure 13(c)), just below the fracture load. Throughout these cycles, minimal changes in slope were observed. There was a slight hysteresis between the load descent and ascent and the filaments exhibited a slight shift in the cycles as they progressed.

Microstructural evaluations were also conducted on the surfaces of highly deformed filaments (Figure 14). In Figure 14(a), the surface near the edge of a filament printed with a 200 µm nozzle is depicted. This region, which remains undistorted, reveals the presence of large zirconia grains (indicated by blue arrows), small alumina grains (yellow arrows) and strontium aluminate platelets (purple arrows). Moving to Figure 14(b), which represents the center of that filament (zone submitted to highest stress), fine circular streaks can be observed on the zirconia grains (highlighted in green). These streaks correspond to the crystalline growth of the grains during the sintering process. Additionally, twinning is visible (highlighted in red), which is a sure sign that the t-m transformation took place in these grains [50].

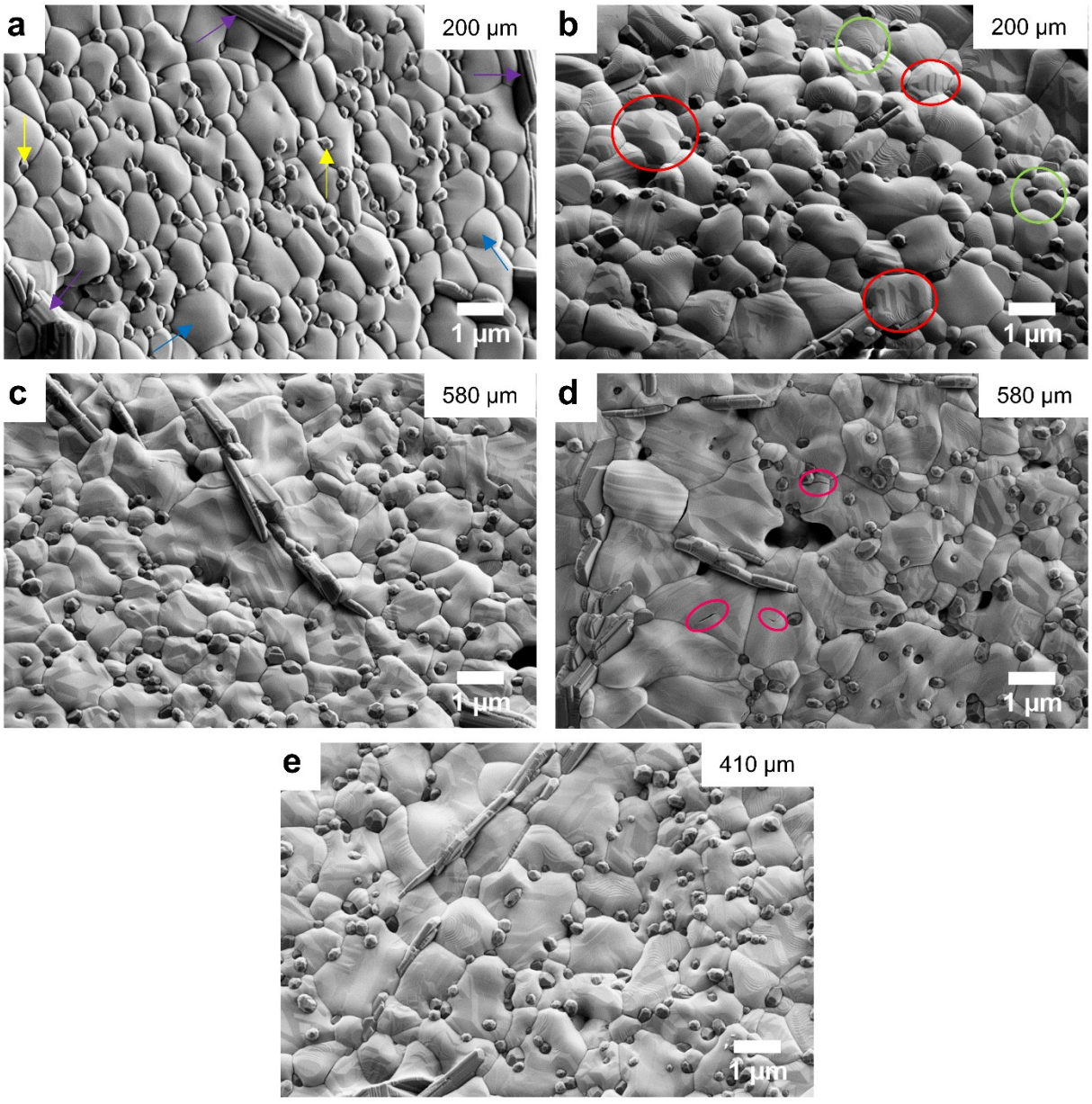

Figure 14. SEM images of highly deformed CS-ATZ filaments. Filament printed with a 200 µm nozzle (a) at the edge of the filament (unloaded zone) and (b) at the center of the filament (zone of maximum tensile stress). (c) Filament printed with a 580 µm nozzle deformed until right before fracture and (d) deformed by cycles of different forces. (e) Filament printed with a 410 µm nozzle deformed by cycles of the same force.

Figure 14(c) and (d) display the surface of a filament printed with a larger diameter (580 µm). Larger zirconia grains were visible surrounding the strontium aluminate platelets, exhibiting a distinct pattern compared to the rest of the material. Additionally, the alumina grains tended to cluster in areas away from the strontium aluminate platelets. The images also revealed the presence of a few pores. Particularly in Figure 14(d), a few microcracks could be observed, highlighted in pink.

The microstructure of a filament printed with a 410 µm nozzle, which underwent flexural cycles with a constant identical imposed load (mechanically evaluated in Figure 13), was also examined. The microstructure is depicted in Figure 14(e). In this image, there was no indicative of an increased presence of microcracks specifically. However, it appeared that the entire material had undergone some t-m transformation. Overall, no significant noticeable differences were observed compared to the other samples.

4. Discussion

Over the past few years, there has been rapid growth in Additive Manufacturing (AM) techniques due to their ability to ease the production of intricate shapes and potentially streamline the manufacturing process. However, the application of AM in ceramics poses several challenges. Unlike metals, ceramics are more susceptible to defects caused during processing, making the AM process less forgiving. Moreover, current AM methods for ceramics often yield larger material defects compared to other established industrial technologies [3]. In the DIW method, increasing the mechanical reliability of the ceramic components obtained has been a challenge.

This study aimed to enhance the mechanical properties and reliability of alumina-toughened zirconia (ATZ) composites. This was pursued through careful debinding and sintering processes, alongside intended carbon nanofiber (CNF) orientation within the composite.

4.1 Challenges of CNF addition

When incorporating carbon nanofibers (CNFs) into a ceramic matrix, three primary challenges need to be addressed: achieving a homogeneous dispersion, achieving proper orientation (if desired, as in the case of this study) and ensuring sintering without inducing thermal degradation of the CNFs. In the following paragraphs, we will discuss each of these challenges.

4.1.1 Homogeneous dispersion of CNFs

Achieving proper dispersion of CNFs within a material presents a significant challenge, as their near-perfect nanostructure makes it very difficult to disperse them into both organic and inorganic materials [51]. In the literature, various strategies have been employed to enhance the dispersion of CNFs and also carbon nanotubes (CNTs) [52], including molecular level mixing, hydrothermal synthesis, ultrasonication [53,54], sol-gel synthesis, use of deflocculants or surfactants [55–57], ball milling and high-speed mixing methods [58,59]. Overall, the CNFs' dispersion is limited by their weight fraction and this limit varies with the dispersion process [52]. In this study, a deflocculant (Darvan® 821-A) was utilized, along with a high-speed mixing technique. Nevertheless, these measures were proved insufficient to deagglomerate the CNFs. For the sequence of the study, it is necessary to explore alternative deflocculants that are more suitable and to improve the deflocculation procedure to achieve better results.

4.1.2 Proper orientation of the CNFs

Direct Ink Writing (DIW) is an additive manufacturing technique that enables the fabrication of intricate three-dimensional structures. It has emerged as a promising method for producing anisotropic materials containing highly oriented phases or particles with high aspect ratios. The orientation behavior observed in DIW aligns with Jeffery's Obit theory [60] and the Folgar-Tucker equation [32], which propose that non-equiaxed particles tend to rotate and align themselves parallel to the shear direction under shear stresses.

It has been observed that the distribution of additions within the extruded filament is not uniform [37]. Fiber orientation and arrangement are more pronounced and denser closer to the nozzle wall, while the middle region exhibits a less orderly and sparser arrangement. This gradient distribution from the filament's center to the wall is attributed to the non-uniform shear rate distribution during extrusion [33]. The distribution patterns differ between Newtonian and non-Newtonian fluids. In the case of Newtonian fluids, there is a linear increase in shear rate from the middle to the edge of the nozzle. On the other hand, non-Newtonian fluids display a non-linear shear rate distribution, with a practically shear-free zone (referred to as the "0" shear rate area) in the center of the nozzle [37]. The width of this "0" shear rate area increases with larger nozzle diameters. Therefore, the potential for orientation in DIW relies on optimizing a balanced combination of factors, which can be summarized as follows [32,37]:

- Particle shape (length/diameter ratio): Higher aspect ratios enhance orientation potential;
- Interaction between particles (solid content): Optimization is required to prevent interference among particles (referred to as the "bridging" effect), avoid nozzle blockage due to excessive particle content, and maintain the desired reinforcement effect;
- Shear rate controlled by nozzle diameter: Decreasing the diameter increases the shear rate. Finding the optimal diameter is crucial to ensure sufficient shear stress and orientation throughout the entire nozzle area, as well as achieve the desired finishing aspects of the printed component;
- Shear time controlled by nozzle length: Increasing the nozzle length prolongs the shear time and can be adjusted in combination with other parameters to achieve proper orientation.

In this study, when considering the particle shape, the added CNFs possess a high aspect ratio (from 150 to 1000.) and, therefore, a good orientation potential, as corroborated by other studies that have reported the orientation of CNFs with DIW [31,36,37]. The solid content utilized (30 vol%) was optimized in another study (data not shown here) and was found to be far from the maximum solid content of the system of the studied paste (47 vol%). The shear time was not varied in this study, but the studies that did achieve CNF orientation utilized the same nozzle length as this study (31 mm) [36] or bigger (50 mm) [37]. The focus of this paper was the variation of the nozzle diameter, ranging from 840 to 200 µm. The latter is estimated by Eq. (1) to induce a considerable shear rate of approximately 400 s^{-1}. Other studies reporting CNF orientation utilized nozzles of a diameter of 500 µm [37], 250, 400 or 610 µm [31] and even 1250 µm [36]. Therefore, it is expected that the diameters employed in this study would also lead to CNF orientation. Nevertheless, no orientation of the CNFs was observed in this study. The primary obstacle in achieving orientation was likely the agglomeration of CNFs, which, once agglomerated, do not experience the same shear forces as individual, deagglomerated CNFs would. The studies that have reported CNF orientation utilized a quantity of 3-15 vol% [31] or even 23 wt% [37] – in this study, the quantities were much lower: 1.34 vol% (equivalent to 0.5 wt%) or 5.23 vol% (2.0 wt%). Hence, the quantity of CNFs is unlikely to be the main issue. The aspect that requires optimization is the deflocculation process.

4.1.3 Sintering with CNFs

After removing the water by drying and the Pluronic by debinding, the printed structure was left with the ATZ particles, which required a sintering process to achieve an adequate level of density. This achieved level of density largely influences the mechanical properties of ceramics, highlighting the importance of the sintering approach and parameters utilized. However, incorporating the CNFs adds a challenge to this process.

Traditional sintering methods for carbon nanofiber-ceramic composites involve the use of high temperatures over prolonged periods [61]. However, such prolonged exposure to high temperatures can lead to damage or destruction of the CNFs, significantly diminishing their reinforcement effect [62]. Previous studies have demonstrated that composites containing a carbon-phase content below 1.5 wt% can be sintered with ceramics (e.g., CNT-alumina) using an air atmosphere furnace, provided an appropriate anti-oxidation sagger (protective fireclay box) and carbon black packing powder [63]. Nevertheless, although there were no significant differences observed in terms of microstructure, composites sintered using Spark Plasma Sintering (SPS) techniques exhibited higher hardness and toughness compared to those sintered in air furnaces [63]. Apart from the temperature issue, sintering

carbon-based phases and oxide ceramic phases together poses challenges, as it necessitates a low-oxygen sintering atmosphere to prevent carbon oxidation, which can potentially degrade the oxide ceramics [64]. Other studies that have used carbon nanofibers as reinforcement performed sintering by hot pressing (1300 °C, 40 MPa [65]; 1300 °C, 41 MPa [40], both in argon with 3Y-TZP matrix material) or SPS (60 MPa, 1400 or 1500 °C) [40]. None of them reported degradation of the CNFs.

To overcome these challenges and retain the integrity of CNF structures while achieving sintering at lower temperatures or shorter durations, the Spark Plasma Sintering (SPS) process was employed in this study. In this process, a pulsed-electric-current passes through a graphitic mold and the sample under vacuum, resulting in a heating rate of approximately 300 °C/min (100 °C/min in this specific study). This rapid heating rate achieved through SPS enables quick completion of the sintering process while minimizing damage to the CNFs. Of the tested approaches, the SPS method was the only one that allowed the preservation of the CNFs, as has been observed in Figure 9, in which their integrity after the SPS process was attested. Furthermore, the addition of CNFs did not present any distinct trend in the sintering procedure, despite the literature suggesting that they could hinder the sintering process by pinning off the grain boundaries [66] or facilitate it by lowering the activation energy, as has been reported with carbon nanotubes in a zirconia matrix [67].

To determine the influence of sintering with the SPS method, conventional sintering (CS) was performed to serve as a control group. The sintering temperatures for both sintering approaches were optimized by density evaluations and microstructural evaluations assessing the overall aspect and grain sizes. In terms of the latter, smaller grain sizes are desirable to achieve higher strength and improved mechanical properties [9] – the grain size has also been reported to be closely related to the wear resistance of Y-TZP and alumina materials [68]. The fracture strength of sintered components containing less than 10 mol% CeO_2 has also been shown to be strongly dependent on grain-size [69]. Although the ATZ powder utilized in this study had 11 mol%, special attention was given to selecting a sintering temperature that maximized the density and minimized the grain size. The results indicated that the higher the sintering temperature, the higher the grain size, a fact that has been reported by other studies [69,70]. In the CS approach, the optimum sintering temperature of the ATZ filaments was 1500 °C, whereas, in the case of SPS, a temperature of 1400 °C was selected for sintering filaments with and without CNFs.

4.2 Comparative of mechanical properties

A schematic illustration of the influence of CNF content, nozzle diameter and sintering method on the mechanical properties evaluated in this study is displayed in Figure 15. The decrease in fracture stress and Young's modulus as the CNF content increases was probably connected to the agglomeration of CNFs within the samples, which created porous regions that act as defects in the material (see Figure 9). Additionally, the reduction in fracture strain can be attributed to the fact that this property is a balance between the two properties mentioned earlier.

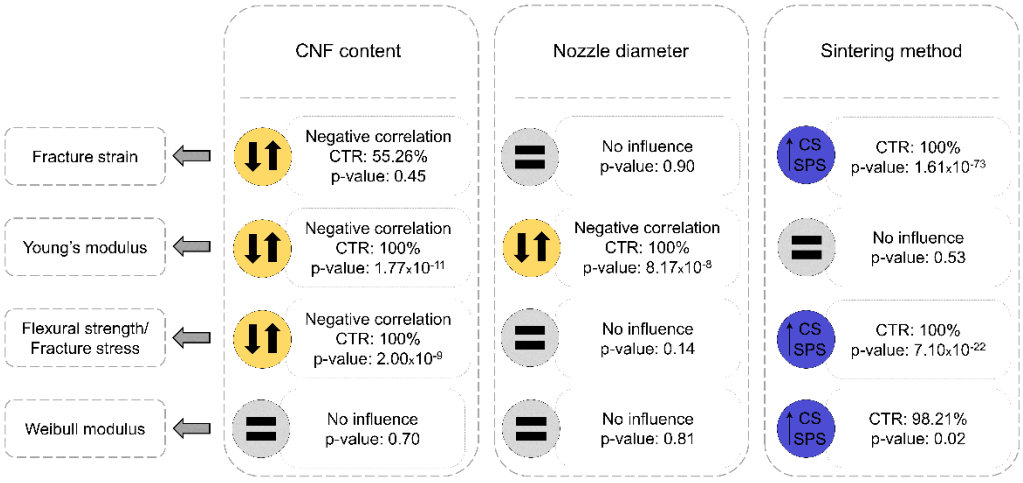

Figure 15. Schematic illustration of the influence of CNF content, nozzle diameter and sintering method on the mechanical properties of the printed filaments. The values obtained from the correlation and regression analyses such as the chance of true relationship (CTR) and p-value are also shown. ***(1.5-column fitting)***

One would expect that reducing the nozzle diameter would lead to an increase in fracture stress due to a size-effect – smaller nozzles produce filaments with reduced volume and, therefore, with a decreased likelihood of defects. Surprisingly, this anticipated trend was not observed. Conversely, smaller nozzle diameters tended to yield filaments with higher Young's modulus, indicating greater stiffness. This outcome likely originated from higher density values of filaments printed using smaller nozzles. When subjected to the same sintering conditions, a sample with less volume would experience more significant densification compared to one with more volume. However, it's important to note that there were no density measurements conducted while varying the nozzle diameter to validate this hypothesis.

The superiority of conventionally sintered samples compared to those subjected to Spark Plasma Sintering (SPS) in terms of fracture strain, fracture stress and Weibull modulus can be attributed to the occurrence of transformation-induced plasticity (TRIP). This phenomenon occurred within the conventionally sintered (CS) samples through t-m transformations, resulting in inelastic deformation. On the other hand, it is hypothesized that the mechanical properties of the SPS samples were hindered due to the presence of a reducing atmosphere within the SPS furnace (primary vacuum). This atmosphere can lead to the creation of oxygen vacancies within the ATZ, reducing the oxides present and thereby hindering the mechanical properties in the SPS-treated samples (as a consequence, the TRIP effect is also unachievable). Usually, the SPS method is utilized with the application of pressure [40], nevertheless, in this study, this was not desirable due to the delicate nature of the printed filaments that would break even under the minimal pressure applied by the SPS (3 N). Hence, a “mini furnace” was created within the SPS equipment to avoid pressure application as depicted by Figure S 2 (Supplementary Material). The filaments were, therefore, exposed to the atmosphere of the furnace, which was unfortunately deleterious to them.

To facilitate comparison with existing literature, Table 4 provides an overview of the processing and sintering methods, as well as the key mechanical properties reported for various materials, including zirconia and ATZ composites, as well as, the materials produced in this study. Comparing the Young’s modulus, the values found in this study are in the same range or higher than those obtained for ATZ (10Ce-TZP/Al_2O_3) via cold isostatic pressing [71,76] and ATZ (10-11.5Ce-TZP/Al_2O_3/$SrAl_{12}O_{19}$) via slip casting [20]. Regarding flexural strength, high values were found in this study. These were in the same range or higher than flexural strength values of all the studies in Table 4 regardless of the processing method (DIW, CIP or SC) and also in comparison to same-composition-ATZ obtained both by slip casting [20] and DIW in previous studies [3].

Finally, the main issue that has been found in most components printed via DIW is the lack of mechanical reliability, which can be translated into low Weibull modulus. The Weibull modulus is a measure of the material's reliability and its value can vary based on the inherent properties of the material, the testing methodology employed and the intended use of the ceramic in practical applications [78]. In general, high Weibull modulus values above 10 or even 20 are considered to indicate good mechanical reliability and strength in ceramics [78]. Usually, the Weibull moduli obtained from ceramics produced through additive manufacturing are lower than those obtained by conventional ceramic processing methods. Indeed, DIW leads to a wider distribution of defects and consequently lower robustness compared to more established ceramic technologies [79,80]. That would raise concerns for structural applications that demand minimal risk of failure. Still, the results found in this study show that a good level of mechanical reliability is achievable by DIW. The obtained values of Weibull modulus were found to be higher than DIW-produced ATZ (3Y-TZP/Al_2O_3) [75], as well as ATZ obtained by CIP (Y-TZP/Al_2O_3 [74] and 10Ce-TZP/Al_2O_3 [76]). The Weibull moduli found were only lower than those of the same composition ATZ obtained by slip casting (m=60, number of samples=23) [20]. The good Weibull moduli found indicate a lower sensitivity to the presence of defects, which has been attributed to the exceptional toughness imparted by the TRIP effect [76]. This, alongside the other good mechanical properties observed of the ductile Ce-TZP-based composites, demonstrates encouraging potential for DIW of these ceramic materials. However, it is important to note that this study focused on evaluating individual filaments. Printing a complete piece/component introduces greater complexity, as factors like inter-filament distance must be carefully considered in both the x-y plane and the z-direction. Making incorrect choices regarding these parameters may result in porosity, which could hinder the mechanical properties of the final component.

Table 4. *Comparison of the processing methods and properties of different ceramics obtained either by traditional ceramic processing methods or DIW, including the results found in this study. ZTA: zirconia-toughened alumina; CIP: cold isostatic pressing; DIW: direct ink writing; SC: slip casting; HIP: hot isostatic pressing; CS: conventional sintering; Z: zirconia; A: alumina: 3PB: 3-point bending; 4PB: 4-point bending; P-3B: piston-on-three balls. Asterisk (*) indicates a value that was not disclosed if wt% or vol%.*

Material	Processing method	Sintering method and temperature	Density (%)	Grain size (μm)	Young's modulus (GPa)	Flexural strength (MPa)	Testing methodology	Weibull modulus	Sample size (mm)	Number of samples	Ref.
3Y-TZP	CIP	CS; 1475 °C 2h	99.5	0.29	203	945 ± 105	3PB	-	3 × 4 × 40	6	[71]
12Ce-TZP	CIP	CS; 1550 °C 2h	-	3.49	-	273 ± 6	4PB	-	3 × 4 × 45	-	[72]
7-16Ce-TZP	CIP	CS; 1400-1600 °C 2h	99	0.5-2.5	-	350-800	3PB	-	3 × 4 × 4	-	[69]
ZTA	DIW	CS; 1570 °C 6h	97.5-99	0.84-1.31	-	422.5	3PB	-	-	-	[73]
ATZ (Y-TZP/Al_2O_3) 80:20%*	CIP	HIP; 1450 °C 2h 1200 bar	>99.5	0.4	-	793-1163	Biaxial bending	7.3-16.5	Ø36 × 2	30	[74]
ATZ (3Y-TZP/Al_2O_3) 80:20 wt%	DIW	CS; 1600 °C 2h	97.3-98.1	Z:0.63-0.9; A:0.62-0.76	-	530-611	P-3B	4.7-5.1	Ø20 × 5	25	[75]
ATZ (10Ce-TZP/Al_2O_3) 70:30 vol%	CIP	CS; 1440 °C 4h	-	0.25 for both	269	1000	4PB	12.6	4 × 6 × 50	10-20	[76]
ATZ (10Ce-TZP/Al_2O_3) 70:30 vol%	CIP	CS; 1440 °C 4h	-	0.59	247	941 ± 34	3PB	-	3 × 4 × 40	6	[71]
ATZ (10Ce-TZP/Al_2O_3) 70:30 vol%	CIP	CS; 1450 °C 2h	-	Z: 1; A: 0.01-0.1	-	950	4PB	-	-	-	[77]
ATZ (12Ce-TZP/Al_2O_3) 90:10 wt%	CIP	CS; 1550 °C 2h	-	2.49	-	632 ± 34	4PB	-	3 × 4 × 45	-	[72]
ATZ (10-11.5Ce-TZP/Al_2O_3/$SrAl_{12}O_{19}$), 84:8:8 vol%	SC	CS; 1450 °C 1h	99.9	Z: 0.6 ± 0.2; A: 0.3 ± 0.1	216	680-1100	Biaxial bending	60	Ø12-15 × 1.2	23	[20]
ATZ (11Ce-TZP/Al_2O_3/$SrAl_{12}O_{19}$) 84:8:8 vol%	DIW	CS; 1350 °C 1h	86	-	-	850 ± 22	Biaxial bending (P-3B)	-	Ø12 × 1.5	8	[3]
ATZ (11Ce-TZP/Al_2O_3/$SrAl_{12}O_{19}$) 84:8:8 vol%	DIW	CS; 1500 °C 1h	98.04 ± 2	Z: 0.76 ± 0.3; A: 0.22 ± 0.06	172.5-244.2	585.6-1113.2	3PB	9.1-20.1	ØVarying × 25	30	This study
ATZ (11Ce-TZP/Al_2O_3/$SrAl_{12}O_{19}$) 84:8:8 vol%	DIW	SPS; 1400 °C 1h	98.08 ± 2	Z: 0.79 ± 0.5; A: 0.20 ± 0.07	151.3-304.9	296.6-779.4	3PB	5.8-13.7	ØVarying × 25	30	This study

5. Conclusions

Filaments of an ATZ composite (84 vol% Ce-TZP, 8% Al_2O_3, 8% $SrAl_{12}O_{19}$) with and without carbon nanofibers (CNFs) were fabricated using Direct Ink Writing (DIW), an additive manufacturing method. The objective was to enhance the mechanical properties of these composites through careful debinding and sintering processes, as well as the orientation of CNFs induced by the shear associated with the printing nozzles. The nozzle diameter was varied in the range of 200 to 840 μm. Optimal debinding and sintering conditions were determined, utilizing both Conventional Sintering (CS) and Spark Plasma Sintering (SPS) methods. Evaluation of the filaments included mechanical properties such as fracture stress/flexural strength, fracture strain, Young's modulus and mechanical reliability determined by the Weibull modulus.

The addition of the CNFs, which was expected to improve the mechanical properties, had an adverse effect in this study. The negative impact can be attributed to the agglomeration of CNFs, highlighting the need to explore alternative deflocculants and improve the deflocculation procedure for better results. Theoretically, smaller nozzle diameters should promote more uniform fiber alignment and orientation throughout the filament in the longitudinal direction. However, this phenomenon was not observed due to the poor dispersion of CNFs. Nevertheless, printing with smaller nozzles showed improvements in the Young's modulus. Conventionally sintered ATZ samples exhibited transformation-induced plasticity, while those sintered by SPS did not, a fact that led to CS samples presenting higher fracture strains, flexural strengths and Weibull moduli.

The mechanical properties obtained were comparable to or higher than those achieved through conventional ceramic processing techniques like cold isostatic pressing and slip casting. Similarly, the mechanical reliability, which is often a concern with DIW, was also satisfactory. Overall, these results demonstrate the promising potential of DIW for ceramic materials, especially ductile Ce-TZP-based composites.

Acknowledgments

This work was supported by the Higher Education Personnel Improvement Coordination (CAPES/Brazil), in the frame of the CAPES/COFECUB program (project CERCA, process number n°88881.665101/2022-01 (Ph936/19)). The authors would also like to thank the Foundation for the Support of Research and Innovation of the State of Santa Catarina – FAPESC (ref. 2021TR001461), the National Council for Scientific and Technological Development (CNPq-Brazil/442820/2023-2 and 303009/2019-5) and the Higher Education Personnel Improvement Coordination (CAPES-PRINT/88881.310728/2018-01).

CREDITS

Vivian Inês dos Santos: Conceptualization; Data curation; Formal analysis; Investigation; Methodology; Project administration; Supervision; Validation; Visualization; Writing – original draft; Writing – review & editing. **Aziliz Ferey:** Data curation; Formal analysis; Investigation; Visualization; Writing – original draft. **Eva Chevalier:** Data curation; Formal analysis; Investigation. **Márcio Celso Fredel:** Conceptualization; Funding acquisition; Resources. **Bruno Henriques:** Conceptualization; Funding acquisition; Resources. **Laurent Gremillard:** Conceptualization; Funding acquisition; Resources. Supervision; Writing – review & editing.

References

[1] J. Chevalier, L. Gremillard, A. V. Virkar, D.R. Clarke, The tetragonal-monoclinic transformation in zirconia: Lessons learned and future trends, Journal of the American Ceramic Society 92 (2009) 1901–1920. https://doi.org/10.1111/j.1551-2916.2009.03278.x.

[2] J. Chevalier, L. Gremillard, Ceramics for medical applications: A picture for the next 20 years, J Eur Ceram Soc 29 (2009) 1245–1255. https://doi.org/10.1016/j.jeurceramsoc.2008.08.025.

[3] J. Chevalier, A. Liens, H. Reveron, F. Zhang, P. Reynaud, T. Douillard, L. Preiss, V. Sergo, V. Lughi, M. Swain, N. Courtois, Forty years after the promise of «ceramic steel?»: Zirconia-based composites with a metal-like mechanical behavior, Journal of the American Ceramic Society 103 (2020) 1482–1513. https://doi.org/10.1111/jace.16903.

[4] R.C. Garvie, R.H. Hannink, R.T. Pascoe, Ceramic steel?, Nature 258 (1975) 703–704. https://doi.org/10.1038/258703a0.

[5] G. Rauchs, T. Fett, D. Munz, R. Oberacker, Tetragonal-to-monoclinic phase transformation in CeO2-stabilized zirconia under uniaxial loading, J Eur Ceram Soc 21 (2001) 2229–41.

[6] R.A. Cutler, J.M. Lindemann, J.H. Ulvensøen, H.I. Lange, Damage-resistant SrO-doped Ce-TZP/Al2O3 composites, Mater Des 15 (1994) 123–133. https://doi.org/10.1016/0261-3069(94)90111-2.

[7] R.A. Cutler, R.J. Mayhew, K.M. Prettyman, A. V. Virkar, High-Toughness Ce-TZP/Al2O3 Ceramics with Improved Hardness and Strength, Journal of the American Ceramic Society 74 (1991) 179–186. https://doi.org/10.1111/j.1151-2916.1991.tb07315.x.

[8] R.H.J. Hannnink, M. V. Swain, Metastability of the Martensitic Transformation in a 12 mol% Ceria-Zirconia Alloy: I, Deformation and Fracture Observations, Journal of the American Ceramic Society 72 (1989) 90–98. https://doi.org/10.1111/j.1151-2916.1989.tb05959.x.

[9] P. Palmero, M. Fornabaio, L. Montanaro, H. Reveron, C. Esnouf, J. Chevalier, Towards long lasting zirconia-based composites for dental implants. Part I: Innovative synthesis, microstructural characterization and in vitro stability, Biomaterials 50 (2015) 38–46. https://doi.org/10.1016/j.biomaterials.2015.01.018.

[10] M. Fornabaio, P. Palmero, R. Traverso, C. Esnouf, H. Reveron, J. Chevalier, L. Montanaro, Zirconia-based composites for biomedical applications: Role of second phases on composition, microstructure and zirconia transformability, J Eur Ceram Soc 35 (2015) 4039–4049. https://doi.org/10.1016/j.jeurceramsoc.2015.04.027.

[11] J.-F. Tsai, C.-S. Yu, D.K. Shetty, Fatigue Crack Propagation in Ceria-Partially-Stabilized Zirconia (Ce-TZP)-Alumina Composites, Journal of the American Ceramic Society 73 (1990) 2992–3001. https://doi.org/10.1111/j.1151-2916.1990.tb06706.x.

[12] C.-S. Yu, D.K. Shetty, M.C. Shaw, D.B. Marshall, Transformation Zone Shape Effects on Crack Shielding in Ceria-Partially-Stabilized Zirconia (Ce-TZP)-Alumina Composites, Journal of the American Ceramic Society 75 (1992) 2991–2994. https://doi.org/10.1111/j.1151-2916.1992.tb04376.x.

[13] H.K. Schmid, R. Pennefather, S. Meriani, C. Schmid, Redistribution of Ce and La during processing of Ce(La)-TZP/Al2O3 composites, J Eur Ceram Soc 10 (1992) 381–392. https://doi.org/10.1016/0955-2219(92)90012-3.

[14] M. Nawa, S. Nakamoto, T. Sekino, K. Niihara, Tough and strong Ce-TZP/Alumina nanocomposites doped with titania, Ceram Int 24 (1998) 497–506. https://doi.org/10.1016/S0272-8842(97)00048-5.

[15] J. -F Tsai, U. Chon, N. Ramachandran, D.K. Shetty, Transformation Plasticity and Toughening in CeO2-Partially-Stabilized Zirconia–Alumina (Ce-TZP/Al2O3) Composites Doped with MnO, Journal of the American Ceramic Society 75 (1992) 1229–1238. https://doi.org/10.1111/j.1151-2916.1992.tb05562.x.

[16] S. Maschio, G. Pezzotti, O. Sbaizero, Effect of LaNbO4 addition on the mechanical properties of ceria-tetragonal zirconia polycrystal matrices, J Eur Ceram Soc 18 (1998) 1779–1785. https://doi.org/10.1016/S0955-2219(98)00104-6.

[17] M. Miura, H. Hongoh, T. Yogo, S. Hirano, T. Fujll, Formation of plate-like lanthanum-β-Aluminate crystal in Ce-TZP matrix, J Mater Sci 29 (1994) 262–268. https://doi.org/10.1007/BF00356602.

[18] S. Ori, T. Kojima, T. Hara, N. Uekawa, K. Kakegawa, Fabrication of Ce-TZP/Ba hexaaluminate composites using amorphous precursor of the second phase, Journal of the Ceramic Society of Japan 120 (2012) 111–115. https://doi.org/10.2109/jcersj2.120.111.

[19] T. Yamaguchi, W. Sakamoto, T. Yogo, T. Fujii, S.-I. Hirano, In Situ Formation of Ce-TZP/Ba Hexaaluminate Composites, Journal of the Ceramic Society of Japan 107 (1999) 814–819.

[20] H. Reveron, M. Fornabaio, P. Palmero, T. Fürderer, E. Adolfsson, V. Lughi, A. Bonifacio, V. Sergo, L. Montanaro, J. Chevalier, Towards long lasting zirconia-based composites for dental implants: Transformation induced plasticity and its consequence on ceramic reliability, Acta Biomater 48 (2017) 423–432. https://doi.org/10.1016/j.actbio.2016.11.040.

[21] J.J. Beaman, D.L. Bourell, C.C. Seepersad, D. Kovar, Additive Manufacturing Review: Early Past to Current Practice, J Manuf Sci Eng 142 (2020). https://doi.org/10.1115/1.4048193.

[22] M. Bhuvanesh Kumar, P. Sathiya, Methods and materials for additive manufacturing: A critical review on advancements and challenges, Thin-Walled Structures 159 (2021) 107228. https://doi.org/10.1016/j.tws.2020.107228.

[23] Z. Chen, Z. Li, J. Li, C. Liu, C. Lao, Y. Fu, C. Liu, Y. Li, P. Wang, Y. He, 3D printing of ceramics: A review, J Eur Ceram Soc 39 (2019) 661–687. https://doi.org/10.1016/j.jeurceramsoc.2018.11.013.

[24] Z. Chen, X. Sun, Y. Shang, K. Xiong, Z. Xu, R. Guo, S. Cai, C. Zheng, Dense ceramics with complex shape fabricated by 3D printing: A review, Journal of Advanced Ceramics 10 (2021) 195–218. https://doi.org/10.1007/s40145-020-0444-z.

[25] Y. Lakhdar, C. Tuck, J. Binner, A. Terry, R. Goodridge, Additive manufacturing of advanced ceramic materials, Prog Mater Sci 116 (2021) 100736. https://doi.org/10.1016/j.pmatsci.2020.100736.

[26] P. Morgan, Carbon Fibers and Their Composites, CRC Press, 2005. https://doi.org/10.1201/9781420028744.

[27] N. Yazdani, E. Brown, Carbon nanofibers in cement composites, in: Innovative Developments of Advanced Multifunctional Nanocomposites in Civil and Structural Engineering, Elsevier, 2016: pp. 47–58. https://doi.org/10.1016/B978-1-78242-326-3.00003-8.

[28] Y. Zhou, S. Jeelani, T. Lacy, Experimental study on the mechanical behavior of carbon/epoxy composites with a carbon nanofiber-modified matrix, J Compos Mater 48 (2014) 3659–3672. https://doi.org/10.1177/0021998313512348.

[29] S. Maensiri, P. Laokul, J. Klinkaewnarong, V. Amornkitbamrung, Carbon nanofiber-reinforced alumina nanocomposites: Fabrication and mechanical properties, Materials Science and Engineering: A 447 (2007) 44–50. https://doi.org/10.1016/j.msea.2006.08.009.

[30] A. Sayam, A.N.M.M. Rahman, Md.S. Rahman, S.A. Smriti, F. Ahmed, Md.F. Rabbi, M. Hossain, Md.O. Faruque, A review on carbon fiber-reinforced hierarchical composites: mechanical performance, manufacturing process, structural applications and allied challenges, Carbon Letters 32 (2022) 1173–1205. https://doi.org/10.1007/s42823-022-00358-2.

[31] J.P. Lewicki, J.N. Rodriguez, C. Zhu, M.A. Worsley, A.S. Wu, Y. Kanarska, J.D. Horn, E.B. Duoss, J.M. Ortega, W. Elmer, R. Hensleigh, R.A. Fellini, M.J. King, 3D-Printing of Meso-structurally Ordered Carbon Fiber/Polymer Composites with Unprecedented Orthotropic Physical Properties, Sci Rep 7 (2017). https://doi.org/10.1038/srep43401.

[32] F. Folgar, C.L. Tucker, Orientation Behavior of Fibers in Concentrated Suspensions, Journal of Reinforced Plastics and Composites 3 (1984) 98–119. https://doi.org/10.1177/073168448400300201.

[33] Z. Fu, M. Freihart, L. Wahl, T. Fey, P. Greil, N. Travitzky, Micro- and macroscopic design of alumina ceramics by robocasting, J Eur Ceram Soc 37 (2017) 3115–3124. https://doi.org/10.1016/j.jeurceramsoc.2017.03.052.

[34] E. Feilden, C. Ferraro, Q. Zhang, E. Garcia-Tunon, E. D'Elia, F. Giuliani, L. Vandeperre, E. Saiz, 3D Printing bioinspired ceramic composites, Sci Rep 7 (2017). https://doi.org/10.1038/s41598-017-14236-9.

[35] J.P. Lewicki, J.N. Rodriguez, C. Zhu, M.A. Worsley, A.S. Wu, Y. Kanarska, J.D. Horn, E.B. Duoss, J.M. Ortega, W. Elmer, R. Hensleigh, R.A. Fellini, M.J. King, 3D-Printing of Meso-structurally Ordered Carbon Fiber/Polymer Composites with Unprecedented Orthotropic Physical Properties, Sci Rep 7 (2017) 43401. https://doi.org/10.1038/srep43401.

[36] P. Huang, Z. Xia, S. Cui, 3D printing of carbon fiber-filled conductive silicon rubber, Mater Des 142 (2018) 11–21. https://doi.org/10.1016/j.matdes.2017.12.051.

[37] Z. Lu, Y. Xia, K. Miao, S. Li, L. Zhu, H. Nan, J. Cao, D. Li, Microstructure control of highly oriented short carbon fibres in SiC matrix composites fabricated by direct ink writing, Ceram Int 45 (2019) 17262–17267. https://doi.org/10.1016/j.ceramint.2019.05.283.

[38] B. Román-Manso, F.M. Figueiredo, B. Achiaga, R. Barea, D. Pérez-Coll, A. Morelos-Gómez, M. Terrones, M.I. Osendi, M. Belmonte, P. Miranzo, Electrically functional 3D-architectured graphene/SiC composites, Carbon N Y 100 (2016) 318–328. https://doi.org/10.1016/j.carbon.2015.12.103.

[39] S. Kumar, T. Rath, R.N. Mahaling, C.K. Das, Processing and characterization of carbon nanofiber/syndiotactic polystyrene composites in the absence and presence of liquid crystalline polymer, Compos Part A Appl Sci Manuf 38 (2007) 1304–1317. https://doi.org/10.1016/j.compositesa.2006.11.006.

[40] J. Dusza, G. Blugan, J. Morgiel, J. Kuebler, F. Inam, T. Peijs, M.J. Reece, V. Puchy, Hot pressed and spark plasma sintered zirconia/carbon nanofiber composites, J Eur Ceram Soc 29 (2009) 3177–3184. https://doi.org/10.1016/j.jeurceramsoc.2009.05.030.

[41] Q. Dou, A. Abdul Karim, X. Loh, Modification of Thermal and Mechanical Properties of PEG-PPG-PEG Copolymer (F127) with MA-POSS, Polymers (Basel) 8 (2016) 341. https://doi.org/10.3390/polym8090341.

[42] J.A. Griggs, Y. Zhang, Determining the confidence intervals of Weibull parameters estimated using a more precise probability estimator, n.d.

[43] J.A. Lewis, Colloidal processing of ceramics, Journal of the American Ceramic Society 83 (2000) 2341–2359. https://doi.org/10.1111/j.1151-2916.2000.tb01560.x.

[44] T. Yu, Z. Zhang, Q. Liu, R. Kuliiev, N. Orlovskaya, D. Wu, Extrusion-based additive manufacturing of yttria-partially-stabilized zirconia ceramics, Ceram Int (2019) 1–8. https://doi.org/10.1016/j.ceramint.2019.10.245.

[45] H. Jin, D. Jia, Z. Yang, Y. Zhou, Direct ink writing of Si2N2O porous ceramic strengthened by directional β-Si3N4 grains, Ceram Int 46 (2020) 15709–15713. https://doi.org/10.1016/j.ceramint.2020.03.077.

[46] T.J. Hensen, T.G. Aguirre, C.L. Cramer, A.S. Wand, K. Ma, D.A. Prawel, J.D. Williams, T.B. Holland, Additive manufacturing of ceramic nanopowder by direct coagulation printing, Addit Manuf 23 (2018) 140–150. https://doi.org/10.1016/j.addma.2018.07.010.

[47] Z. Goharibajestani, O. Akhlaghi, C. Akaoglu, F. Afghah, N. Khani, A. Hodaei, B. Koc, O. Akbulut, Incorporating Steric Hindrance into the Additive Design Enables a Robust Formulation of Alumina Ink for Extrusion-based 3D Printing, ACS Appl Polym Mater 1 (2019) 3279–3285. https://doi.org/10.1021/acsapm.9b00704.

[48] L. Yang, X. Zeng, Y. Zhang, 3D printing of alumina ceramic parts by heat-induced solidification with carrageenan, Mater Lett 255 (2019) 126564. https://doi.org/10.1016/j.matlet.2019.126564.

[49] Y. Yang, D. Cai, Z. Yang, X. Duan, P. He, D. Jia, Y. Zhou, Rheology of organics-free aqueous ceramic suspensions for additive manufacturing of dense silicon nitride ceramics, Ceram Int 48 (2022) 31941–31951. https://doi.org/10.1016/j.ceramint.2022.07.130.

[50] W.D. Scott, Deformation Twinning in Ceramics, in: Deformation of Ceramic Materials II, Springer US, Boston, MA, 1984: pp. 235–249. https://doi.org/10.1007/978-1-4615-6802-5_17.

[51] B. Dorj, J.-E. Won, J.-H. Kim, S.-J. Choi, U.S. Shin, H.-W. Kim, Robocasting nanocomposite scaffolds of poly(caprolactone)/hydroxyapatite incorporating modified carbon nanotubes for hard tissue reconstruction, J Biomed Mater Res A 101A (2013) 1670–1681. https://doi.org/10.1002/jbm.a.34470.

[52] K.K. Kar, Composite materials: Processing, applications, characterizations, Composite Materials: Processing, Applications, Characterizations (2016) 1–686. https://doi.org/10.1007/978-3-662-49514-8.

[53] F. Ye, L. Liu, Y. Wang, Y. Zhou, B. Peng, Q. Meng, Preparation and mechanical properties of carbon nanotube reinforced barium aluminosilicate glass–ceramic composites, Scr Mater 55 (2006) 911–914. https://doi.org/10.1016/j.scriptamat.2006.07.045.

[54] C. Balázsi, B. Fényi, N. Hegman, Z. Kövér, F. Wéber, Z. Vértesy, Z. Kónya, I. Kiricsi, L.P. Biró, P. Arató, Development of CNT/Si3N4 composites with improved mechanical and electrical properties, Compos B Eng 37 (2006) 418–424. https://doi.org/10.1016/j.compositesb.2006.02.006.

[55] J. Sun, L. Gao, X. Jin, Reinforcement of alumina matrix with multi-walled carbon nanotubes, Ceram Int 31 (2005) 893–896. https://doi.org/10.1016/j.ceramint.2004.10.002.

[56] J. Sun, L. Gao, W. Li, Colloidal processing of carbon nanotube/alumina composites, Chemistry of Materials 14 (2002) 5169–5172. https://doi.org/10.1021/cm020736q.

[57] N. Garmendia, I. Santacruz, R. Moreno, I. Obieta, Slip casting of nanozirconia/MWCNT composites using a heterocoagulation process, J Eur Ceram Soc 29 (2009) 1939–1945. https://doi.org/10.1016/j.jeurceramsoc.2008.12.014.

[58] S. Maensiri, P. Laokul, J. Klinkaewnarong, V. Amornkitbamrung, Carbon nanofiber-reinforced alumina nanocomposites: Fabrication and mechanical properties, Materials Science and Engineering: A 447 (2007) 44–50. https://doi.org/10.1016/j.msea.2006.08.009.

[59] Cs. Balázsi, F. Wéber, Zs. Kövér, Z. Shen, Z. Kónya, Zs. Kasztovszky, Z. Vértesy, L.P. Biró, I. Kiricsi, P. Arató, Application of carbon nanotubes to silicon nitride matrix reinforcements, Current Applied Physics 6 (2006) 124–130. https://doi.org/10.1016/j.cap.2005.07.024.

[60] G.B. Jeffery, P.R.S.L. A, The motion of ellipsoidal particles immersed in a viscous fluid, Proceedings of the Royal Society of London. Series A, Containing Papers of a Mathematical and Physical Character 102 (1922) 161–179. https://doi.org/10.1098/rspa.1922.0078.

[61] J.-P. Fan, D.-M. Zhuang, D.-Q. Zhao, G. Zhang, M.-S. Wu, F. Wei, Z.-J. Fan, Toughening and reinforcing alumina matrix composite with single-wall carbon nanotubes, Appl Phys Lett 89 (2006) 121910. https://doi.org/10.1063/1.2336623.

[62] A. Duszová, J. Dusza, K. Tomášek, G. Blugan, J. Kuebler, Microstructure and properties of carbon nanotube/zirconia composite, J Eur Ceram Soc 28 (2008) 1023–1027. https://doi.org/10.1016/j.jeurceramsoc.2007.09.011.

[63] J. Sun, M. Iwasa, T. Nakayama, Þ.K. Niihara, L.G.A.O. Þ, X.J.I.N. Þ, Pressureless Sintering of Alumina Carbon Nanotubes Composites in Air Atmosphere Furnace and Their Mechanical Properties, 406 (2004) 403–406.

[64] L. Gremillard, J. Chevalier, T. Epicier, G. Fantozzi, Improving the Durability of a Biomedical-Grade Zirconia Ceramic by the Addition of Silica, Journal of the American Ceramic Society 85 (2002) 401–7.

[65] A. Duszová, J. Dusza, K. Tomášek, J. Morgiel, G. Blugan, J. Kuebler, Zirconia/carbon nanofiber composite, Scr Mater 58 (2008) 520–523. https://doi.org/10.1016/j.scriptamat.2007.11.002.

[66] M. Mazaheri, D. Mari, R. Schaller, G. Bonnefont, G. Fantozzi, Processing of yttria stabilized zirconia reinforced with multi-walled carbon nanotubes with attractive mechanical properties, J Eur Ceram Soc 31 (2011) 2691–2698. https://doi.org/10.1016/j.jeurceramsoc.2010.11.009.

[67] B. Milsom, G. Viola, Z. Gao, F. Inam, T. Peijs, M.J. Reece, The effect of carbon nanotubes on the sintering behaviour of zirconia, J Eur Ceram Soc 32 (2012) 4149–4156. https://doi.org/10.1016/j.jeurceramsoc.2012.07.028.

[68] K.-H. Zum Gahr, W. Bundschuh, B. Zimmerlin, Effect of grain size on friction and sliding wear of oxide ceramics, Wear 162–164 (1993) 269–279. https://doi.org/10.1016/0043-1648(93)90509-K.

[69] K. Tsukuma, Strength, fracture toughness and Vickers hardness of CeO2-stabilized tetragonal Zr02 polycrystals (Ce-TZP), J Mater Sci 20 (1985) 1178–1184.

[70] D. Glymond, L.J. Vandeperre, Robocasting of MgO-doped alumina using alginic acid slurries, Journal of the American Ceramic Society 101 (2018) 3309–3316. https://doi.org/10.1111/jace.15509.

[71] K. Tanaka, J. Tamura, K. Kawanabe, M. Nawa, M. Oka, M. Uchida, T. Kokubo, T. Nakamura, Ce-TZP/Al2O3 nanocomposite as a bearing material in total joint replacement, J Biomed Mater Res 63 (2002) 262–270. https://doi.org/10.1002/jbm.10182.

[72] J.-F. Tsai, U. Chon, N. Ramachandran, D.K. Shetty, Transformation Plasticity and Toughening in CeO2-Partially-Stabilized Zirconia-Alumina (Ce-TZP/Al2O3) Composites Doped with MnO, Journal of the American Ceramic Society 75 (1992) 1229–1238. https://doi.org/10.1111/j.1151-2916.1992.tb05562.x.

[73] T. Yu, X. Zhu, H. Yu, P. Wu, C. Li, X. Han, M. Chen, Material extrusion-based additive manufacturing of zirconia toughened alumina: Machinability, mechanical properties and biocompatibility, J Manuf Process 94 (2023) 120–132. https://doi.org/10.1016/j.jmapro.2023.03.052.

[74] S. Begand, T. Oberbach, W. Glien, Investigations of the Mechanical Properties of an Alumina Toughened Zirconia Ceramic for an Application in Joint Prostheses, Key Eng Mater 284–286 (2005) 1019–1022. https://doi.org/10.4028/www.scientific.net/KEM.284-286.1019.

[75] N.R.M. Lévaro, M.F.R.P. Alves, C. Santos, V. Sencadas, S. Olhero, Direct ink writing of ATZ composites based on inks prepared by colloidal or hydrogel route: Linking inks rheology with mechanical properties, Colloids Surf A Physicochem Eng Asp 668 (2023) 131426. https://doi.org/10.1016/j.colsurfa.2023.131426.

[76] R. Benzaid, J. Chevalier, M. Saâdaoui, G. Fantozzi, M. Nawa, L.A. Diaz, R. Torrecillas, Fracture toughness, strength and slow crack growth in a ceria stabilized zirconia-alumina nanocomposite for medical applications, Biomaterials 29 (2008) 3636–3641. https://doi.org/10.1016/j.biomaterials.2008.05.021.

[77] M. Nawa, N. Kurizoe, Y. Okamoto, A. Ueno, Transformation-induced plastic deformation in Ce-TZP/alumina nanocomposite generated during fatigue tests at room temperature, J Eur Ceram Soc 34 (2014) 4337–4345. https://doi.org/10.1016/j.jeurceramsoc.2014.06.025.

[78] W. Weibull, A Statistical Theory of the Strength of Materials, Generalstabens Litografiska Anstalts Förlag, Stockholm, 1939.

[79] E. Feilden, E.G.T. Blanca, F. Giuliani, E. Saiz, L. Vandeperre, Robocasting of structural ceramic parts with hydrogel inks, J Eur Ceram Soc 36 (2016) 2525–2533. https://doi.org/10.1016/j.jeurceramsoc.2016.03.001.

[80] M. Maillard, J. Chevalier, L. Gremillard, G.P. Baeza, E.J. Courtial, S. Marion, V. Garnier, Optimization of mechanical properties of robocast alumina parts through control of the paste rheology, J Eur Ceram Soc 43 (2023) 2805–2817. https://doi.org/10.1016/j.jeurceramsoc.2022.12.008.

Supplementary Material

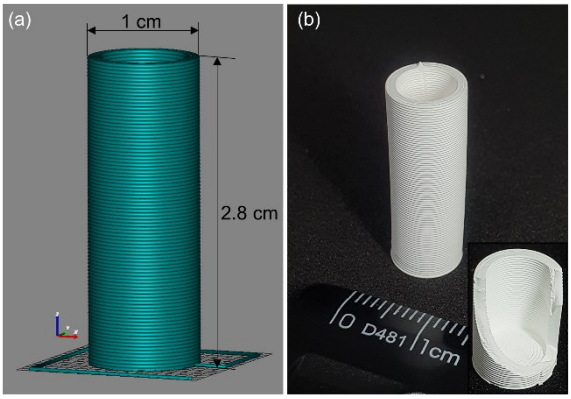

Figure S 1. Alumina crucible into which the filaments were placed after drying to reduce the need to handle them and prevent their breakage. (a) CAD model and (b) photograph of the crucibles – inset photograph of (b) shows a broken crucible to better observe its bottom configuration. Since one of the main advantages of the DIW technique is its versatility in terms of shape creation with ceramics, it seemed natural to produce the crucibles by DIW. Nozzles of 410 µm were used and the crucibles had 1 cm of diameter with 2.8 cm of height. The first five layers were designed to be fully printed whereas the subsequent layers were hollow.

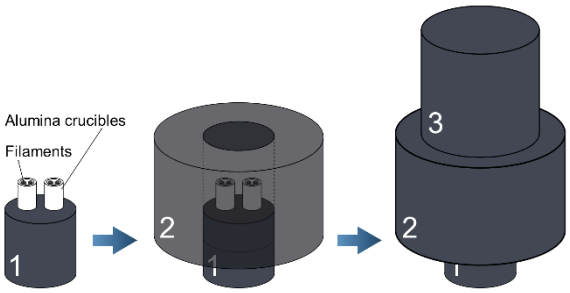

Figure S 2. Schematic illustration of the configuration of the samples within the SPS furnace to avoid the application of pressure.